

1 **The growth of faults and fracture networks in a mechanically
2 evolving, mechanically stratified rock mass: A case study from
3 Spireslack Surface Coal Mine, Scotland**

4 Billy J. Andrews*, Zoe K. Shipton, Richard Lord, Lucy McKay

5 Department of Civil and Environmental Engineering, University of Strathclyde, Glasgow, G11XJ,
6 Scotland

7 *Correspondence to:* Billy J. Andrews (billy.andrews@strath.ac.uk)

8 **Abstract.**

9 Fault architecture and fracture network evolution (and resulting bulk hydraulic properties) are highly
10 dependent on the mechanical properties of the rocks at the time the structures developed. This paper
11 investigates the role of mechanical layering and pre-existing structures on the evolution of strike-slip
12 faults and fracture networks. Detailed mapping of exceptionally well exposed fluvial-deltaic lithologies
13 at Spireslack Surface Coal Mine, Scotland, reveals two phases of faulting with an initial sinistral, and
14 later dextral, sense of shear with ongoing pre-, syn- and post-faulting joint sets. We find fault zone
15 internal structure depends on whether the fault is self-juxtaposed or cuts multiple lithologies, the
16 presence of shale layers which promote bed-rotation and fault-core lens formation, and the orientation
17 of joints and coal cleats at the time of faulting. During ongoing deformation, cementation of fractures is
18 concentrated where the fracture network is most connected. This leads to the counter-intuitive result that
19 the highest fracture density part of the network often has the lowest open fracture connectivity. To
20 evaluate the final bulk hydraulic properties of a deformed rock mass it is crucial to appreciate the
21 relative timing of deformation events, concurrent or subsequent cementation, and the interlinked effects
22 on overall network connectivity.

23 **1 Introduction**

24 Differences in the mechanical properties (mechanical stratigraphy) of rock layers have long been
25 recognised as influencing the style and evolution of faults (Anderson, 1951; Donath, 1961; Ranalli and
26 Yin, 1990; Ferrill et al., 2017)). However, work has tended to focus particularly on normal faults, with
27 the effect of mechanical layers in sand-shale sequences (e.g. van der Zee & Urai (2005); Schmatz *et al.*
28 (2010)), interbedded limestones and marls (e.g. Ferrill & Morris (2003), (2008); Long & Imber (2011);
29 Ferrill *et al.* (2012)), and ignimbrites (Soden and Shipton, 2013) receiving particular attention. The
30 lithology being cut by the fault influences fault dip: strands in competent layers have steeper dips than
31 those in incompetent layers (Ferrill and Morris, 2008) with important consequences for vein geometry
32 and mineralisation potential (Dunham 1948). The ratio of competent to incompetent lithologies thus
33 affects fault style and displacement profiles (Ferrill et al., 2017; Ferrill and Morris, 2008). Fault-related
34 folding of thin competent layers (e.g. limestones) is common in successions otherwise dominated by
35 incompetent lithologies (e.g. shale) (Ferrill and Morris, 2008; Lăpădat et al., 2017). The presence of
36 incompetent lithologies also restricts fault growth with strands terminating at incompetent beds and
37 leads to formation of faults with high length to height ratios orientated parallel to the strike of bedding
38 (e.g. Nicol *et al.* (1996); Soliva & Benedicto (2005); Roche *et al.* (2013)).

39 Pre-existing weaknesses (e.g., joints and faults) also play an important role in the nucleation,
40 orientation, and length of later faults (Crider and Peacock, 2004; Peacock, 2001; Walsh *et al.*, 2002).
41 The mechanical response of a pre-existing joint to faulting will depend on the orientation of the feature
42 relative to far field stress (Moir et al., 2010), the ratio of principal stresses (Lunn et al., 2008; Healy et
43 al., 2006; Moir, 2010; Chang and Haimson, 2000; Haimson and Chang, 2000), and local variations in
44 the stress field due to the interaction of joints in the pre-existing network (Crider and Peacock, 2004;
45 Kattenhorn et al., 2000; Moir et al., 2010; Peacock, 2001). Where joints or cleats are orientated
46 perpendicular to the growth direction of faults, they can act as a strength contrast and restrict fault
47 growth (Wilkins and Gross, 2002). Alternatively, where pre-existing joints are orientated favourably,
48 they can act as a plane of weakness and be reactivated to form faulted joints (e.g. Crider and Peacock,
49 2004; Cruikshank et al., 1991; Wilkins et al., 2001).

50 Veins are often associated with faulting, providing evidence of the paleo-fluid flow through a fracture
51 network (Bons et al., 2012; Oliver and Bons, 2001; Peacock and Sanderson, 2018) and may act as a
52 baffle to post-cementation basinal fluid flow (e.g. Skurtveit et al., 2015). Additionally, the strength of a
53 rock mass can vary depending on the strength ratio between the host-rock and veins, along with the
54 mineralogy, thickness, and orientation of veins relative to the maximum compressive stress (e.g. Shang
55 et al., 2016; Turichshev and Hadjigeorgiou, 2016, 2017; Virgo et al., 2014). Therefore, the cementation

56 of faults and joints can influence subsequent deformation of the rock mass (Caputo and Hancock, 1998;
57 Holland and Urai, 2010; Ramsay, 1980; Virgo et al., 2013, 2014).

58 Coal-bearing, fluvial-deltaic sequences are commonly mechanically stratified. Fluvial-deltaic sequences
59 are characterised by cyclical sequences of limestone, sandstone, siltstone, seat-earth (paleosols that are
60 often found beneath coal seams), shale and coal (Thomas, 2013, *and references therein*). The competent
61 lithologies in the sequence (limestone and sandstone) commonly contain joints. Coal has a distinctive
62 blocky texture due to the presence of two roughly perpendicular fracture sets referred to as cleats
63 (Laubach et al., 1998). Cleats form in coal beds during diagenesis and act as pre-existing weaknesses
64 that can influence the location, orientation and length of faults.

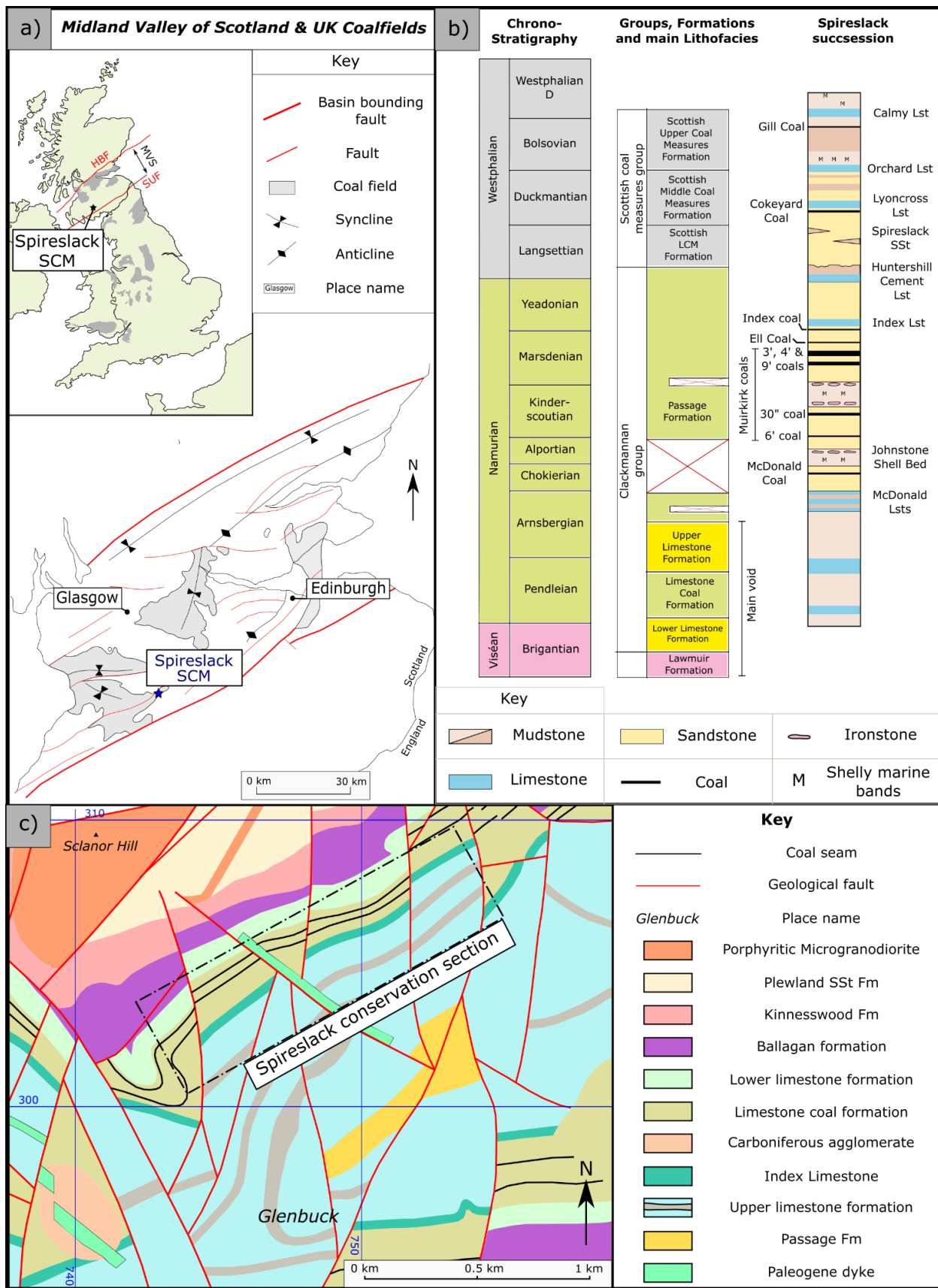
65 This study utilises exceptional fluvial-deltaic exposures of the Limestone Coal Formation exhumed at
66 the Spireslack Surface Coal Mine, Scotland, in order to investigate the effect of lithology, pre-existing
67 structures and synchronous cementation on the evolution of strike-slip faults. Field photographs were
68 used to map the key structures and kinematics at a 1:1,000 scale. High resolution photomontages were
69 then used to map faults and fractures in order to investigate the interaction between faults, lithology,
70 and jointing. We investigate how the internal structure of strike-slip faults at Spireslack Surface Coal
71 Mine depends on the lithology (e.g., the presence of shale) and the presence of pre-existing weaknesses
72 (e.g., joints, cleats). Our observations contrast small offset, self-juxtaposed faults and faults with larger
73 offsets that cut multiple lithologies. Here we attempt to apply the terminology used in fault sealing
74 studies (e.g. Gibson and Bentham, 2003; Knai and Knipe, 1998; Pei et al., 2015; Yielding et al., 2011)
75 in which a self-juxtaposed fault is a fault where the offset is small enough with respect to the layer
76 thickness that the same layer is present on either side.

77 **2. Geological setting**

78 Spireslack Surface Coal Mine is located in the Midland Valley of Scotland. The Midland Valley is a 90
79 km wide, 150 km long, ENE-trending basin that opened during the late Devonian to Early
80 Carboniferous in response to back-arc extension within the Laurussian Plate (Leeder, 1982, 1988). This
81 was followed by a period of thermal subsidence which continued throughout Namurian and
82 Westphalian times leading to the deposition and preservation of thick coal measures across much of the
83 UK (Figure 1a) (Leeder, 1982).

84 The Midland Valley is bound by two major faults; the Southern Upland Fault to the south and Highland
85 Boundary Fault to the north (Figure 1a) (Bluck, 1984). Carboniferous basins that have axes oblique to
86 the main trend of the Midland Valley (e.g. Central Scottish Coalfield; Francis (1991)) can reach over 6

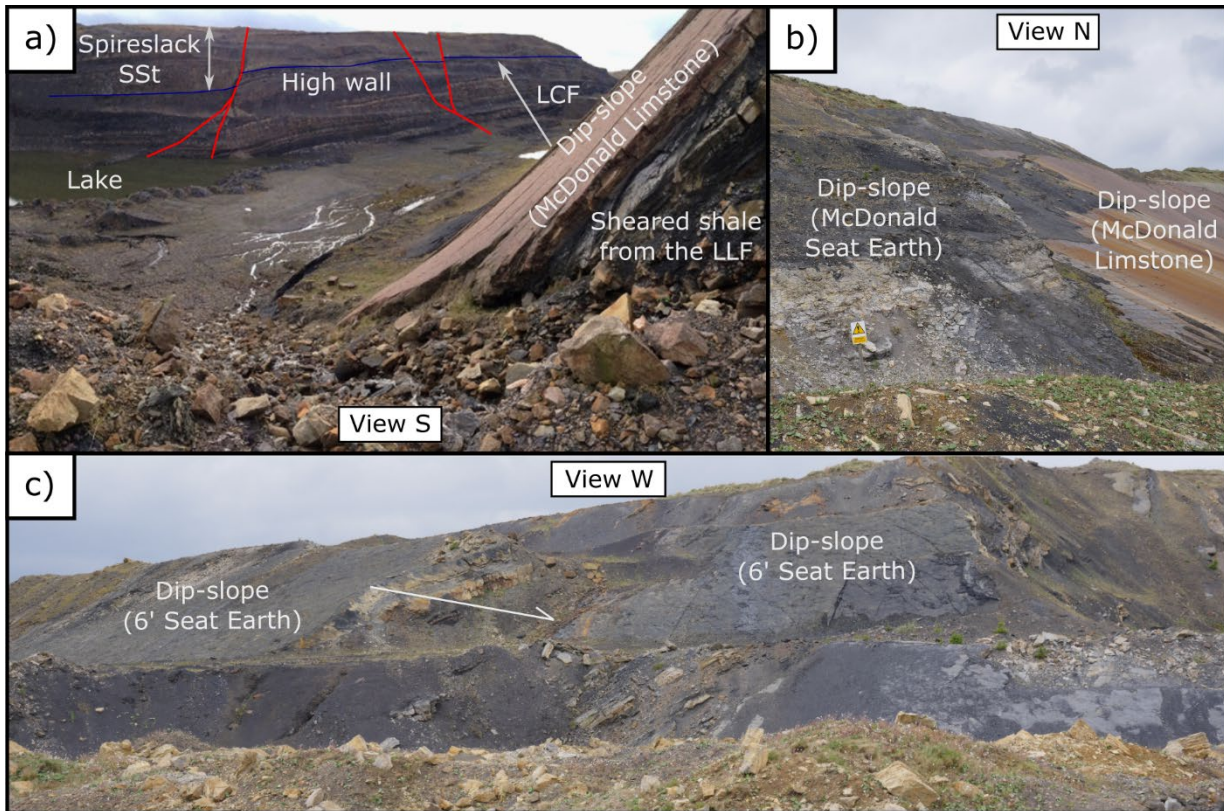
87 km in thickness (Dean et al., 2011) and are often obscured by Quaternary deposits. Faults with
88 associated, localised folding within the Midland Valley have a complex history of reactivation caused
89 by sinistral strike-/oblique-slip movement during the Tournaisian and dextral strike-/oblique-slip
90 movement during Viséan to Westphalian times (Browne and Monro, 1987; Rippon et al., 1996; Ritchie
91 et al., 2003; Underhill et al., 2008).



92

93 **Figure 1: Location map: a) Map of UK coalfields (adapted from Donnelly (2006)) showing the**
94 **location of Spireslack Surface Coal Mine (SCM) and structural features of the Midland Valley of**
95 **Scotland; b) Regional geology and c) stratigraphy of Spireslack open cast coal mine (after Ellen et**
96 **al. (2019)).**

97 2.1 Spireslack Surface Coal Mine



98

99 **Figure 2: Overview photographs of Spireslack SCM: a) Photograph from the east of the site of the**
100 **high wall with the McDonald Limestone dip slope visible to the right in the foreground; b)**
101 **photograph looking down the McDonald Limestone pavement from the entrance roadway c)**
102 **Photograph of the 6' Seat Earth exposed in the dip-slope to the west of the site.**

103 Spireslack Surface Coal Mine (SCM), next to the now abandoned coal mining village of Glenbuck in
104 South Ayrshire, Scotland (Figure 1a) provides an exceptional exposure of Carboniferous rocks in a 1
105 km long residual void (Figure 2 & 1c). Shallow, southerly dipping (20° - 40°) bedding planes (dip-
106 slopes) end in a <130 m high working face (the high wall) (Figure 2). The high wall represents the
107 unexcavated working face exposed through the opencast operations, with bedding planes (e.g. the
108 McDonald Limestone) used as the void's dip-slopes.

109 The stratigraphy is comprised of a continuous succession of Viséan to Namurian strata, including a
110 complete section through the Limestone Coal Formation (LCF) (Figure 1b, c) (Ellen et al., 2016, 2019).
111 Bituminous coal is found in cyclical fluvio-deltaic sequences that outcrop across much of the dip-slope
112 and high wall, bounded by the Upper and Lower Limestone Formations. The Lower Limestone
113 Formation represents more marine-influenced facies including extensive, fossil-rich limestone units
114 (e.g. the McDonald Limestone) (Davis, 1972). The Spireslack Sandstone is exposed above the
115 Limestone Coal Formation and comprises of one channelised and two tabular sandstone beds (Ellen et
116 al., 2019).

117 Several faults with shallow slip vectors and variably complex internal structures offset the stratigraphy.
118 Additionally, at least five Paleogene basaltic dykes are observed trending NW-SE to WNW-ESE, which
119 Leslie *et al.* (2016) suggest intrude along pre-existing faults. The rocks exposed at Spireslack SCM are
120 part of the southern limb of the upright, WSW-ENE trending Muirkirk syncline that formed in response
121 to mid- to late- Carboniferous sinistral transpression (Davis, 1972; Leslie *et al.*, 2016). Leslie *et al.*
122 (2016) attribute the faulting and folding observed at Spireslack SCM to this deformation, and have
123 observed no evidence at the site of the later widespread dextral deformation found elsewhere in the
124 Midland Valley (e.g. Underhill *et al.* (2008)).

125 **3. Methods**

126 **3.1. Field mapping**

127 Geological mapping of the dip-slopes captured all sandstone and shale units below the McDonald
128 Limestones and the sandstone bed above the Muirkirk 6' Coal. Mapping was undertaken at a 1:1,000
129 scale onto printed aerial photography from Bing Maps (Microsoft, 2017). All faults with >0.2 m
130 stratigraphic separation were recorded. Printed field photographs were used to collect more detailed
131 observations at several key sites.

132 **3.2 Lineament mapping and network analysis**

133 One way to describe the topology of a fault or fracture network is as a series of branches and nodes (e.g.
134 Manzocchi 2002; Sanderson & Nixon, 2015; 2018). A branch is a fracture trace with a node at each end.
135 Nodes can occur where a fracture terminates into rock (I-node), abuts against another fracture (Y-node)
136 or crosses another fracture (X-node). The proportion of different node types (I, Y, and X) can then be
137 plotted on a triangular diagram to characterise the connectivity of the network (Manzocchi, 2002;
138 Sanderson and Nixon, 2015). In this work we recorded faults and fractures as orientation sets and report
139 fracture/branch trace length (tl), 2D fracture intensity (I), and the percentage of connected branches (Pc,
140 see Equation 1).

141 Fault and fracture mapping were undertaken using two datasets: (i) a drone derived photomontage of the
142 McDonald Limestone bedding plane provided by Dave Healy of Aberdeen University; and (ii) an auto-
143 rectified photomontage of the high wall collected by the British Geological Survey. In order to
144 understand the geometry, topological properties and crosscutting relationships of fault strands/joint sets,
145 interpretation areas were selected from both the dip-slope and high wall for analysis. Due to its
146 instability the high wall is generally unsafe to access, so any interpretations of the high wall are made
147 principally on the photomontage. We outline our workflow in detail below:

148 1. *Lineament mapping*: Field mapping was undertaken by the lead author at a scale of 1:30 for the
 149 dip-slope and 1:50 for the high wall. Scanned field maps were georeferenced and scaled in
 150 ArcGIS. Digitisation of the mapped lineaments, and correlation of features between well exposed
 151 areas, was undertaken by the same person to limit the effect of subjective bias (Andrews et al.,
 152 2019; Scheiber et al., 2015). The faults and the fractures were digitised into separate GIS layers,
 153 with reference to field notebooks and maps to ensure interpretations honoured the field data. While
 154 in the detailed field investigation areas it was possible to distinguish shear fractures from joints,
 155 this was not possible for much of the area. Therefore, both potential shear fractures and joints
 156 were included in the ‘joint’ dataset when in inaccessible areas. The fault and joint datasets were
 157 then merged in ArcGIS, to create a third dataset: the ‘combined network’. The fault, joint, and
 158 combined datasets were then investigated separately, using a network analysis outlined in steps 2
 159 to 4.

160 2. *Define sets*: Six ‘interpretation boxes’ that cover a range of deformation styles and fracture
 161 intensity were defined as shape files in ArcGIS (three along the dip-slope and three along the
 162 high wall). The orientation of faults and fractures within them were then analysed. Length-
 163 weighted rose diagrams with 5° bin widths were used to interpret the orientation sets in the
 164 network using the NetworkGT toolbox (Nyberg et al., 2018).

165 3. *Branch & Nodes*: The topology of the network was then extracted using the ‘Branch and Node’
 166 tool in NetworkGT, which splits the fracture trace poly-line file into individual branches, and
 167 assigns I, Y or X nodes as a separate point-files (Nyberg et al., 2018). The resulting network was
 168 visually checked for errors (e.g. incorrectly assigned nodes) and manually adjusted in ArcGIS to
 169 remove spurious nodes and branches. Data were then exported to Excel for further analysis.

170 4. *Network analysis*: For each network, the following data were extracted;

171 a. *Network connectivity*: For each dataset, with the data not split into sets, the node and
 172 branch proportions were assessed using a triangular diagram (c.f. Sanderson & Nixon
 173 (2015)). From the number of I (N_i), Y (N_y) and X (N_x) nodes, the proportion of
 174 connected branches was then calculated using Equation 1 (Sanderson and Nixon, 2015):

$$P_c = \frac{(3N_y + 4N_x)}{(N_i + 3N_y + 4N_x)} \quad (\text{Equation 1})$$

176 b. *Trace length*: The trace length of digitised networks and sets within each sample area
 177 were assessed using trace length distributions (Priest and Hudson, 1981), with the
 178 minimum, maximum, and median trace length values used to compare analysis.

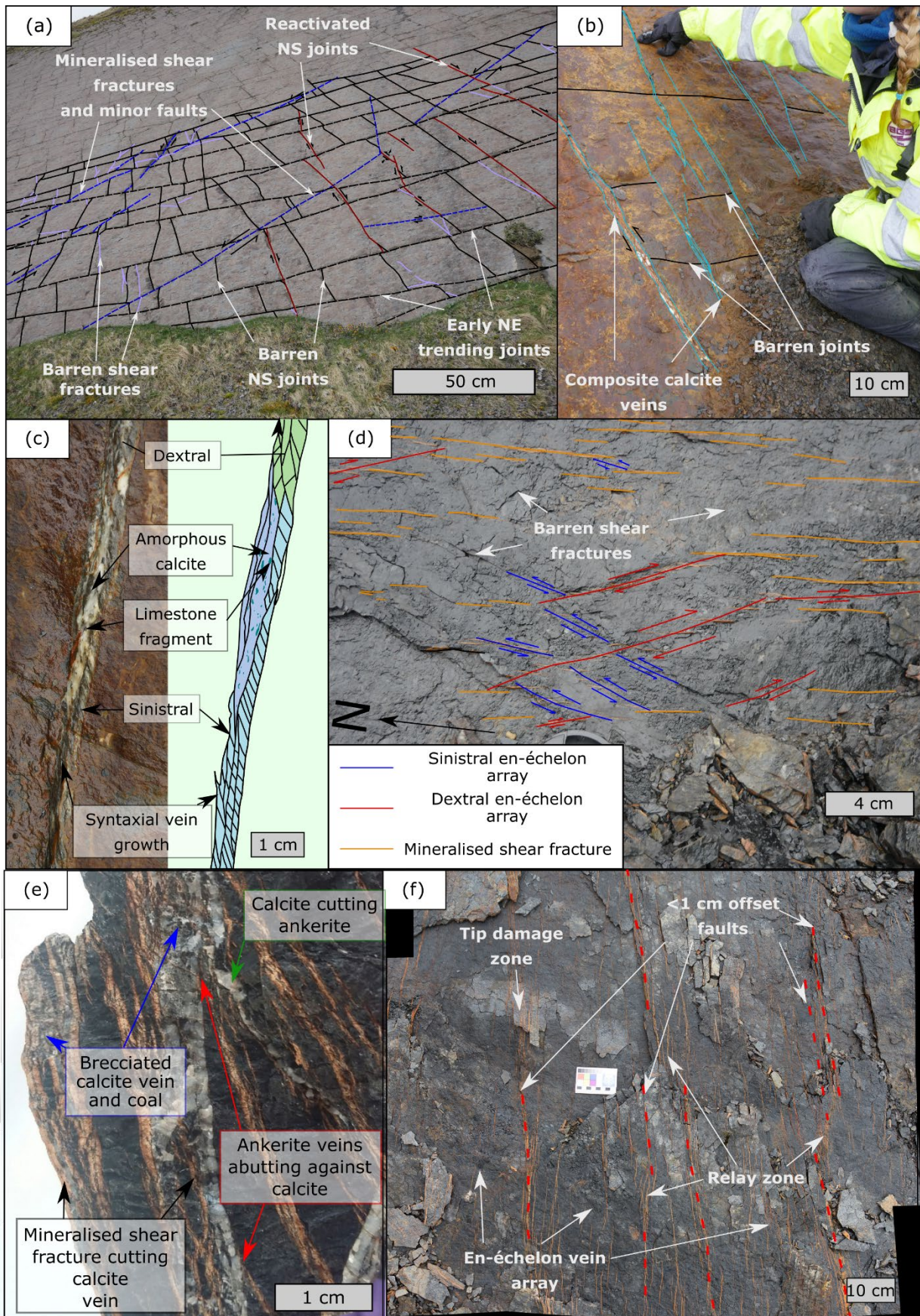
179 c. *2D fracture intensity*: We compared the intensity of the networks and sets within the
180 network using 2D fracture intensity (Equation 2) (P₂₁; Dershowitz & Einstein (1988);
181 Rohrbaugh *et al.* (2002)).

182
$$P_{21} = \frac{\sum tl}{Area} \quad (fractures / m) \quad (Equation \ 2)$$

183 $\sum tl = sum \ of \ all \ fracture \ trace \ lengths, Area = sample \ area$

184 4. Fault and fracture observations

185 4.1 General fracture observations



187 **Figure 3: Typical fracture properties for McDonald Limestone & McDonald Coal: a) joints**
188 **observed away from faults across the southerly dipping (c. 40°) McDonald Limestone bedding**
189 **plane; b) Mineralised N-S trending calcite veins, offsetting abutting E-W ladder joints on the**
190 **bedding plane of the McDonald Limestone; c) annotated field photograph and interpretation of a**
191 **multi-phase composite calcite vein exposed in the vicinity to a small stratigraphic separation fault**
192 **along the McDonald Limestone Pavement; d) bedding plane exposure of mineralised fractures**
193 **present within the Muirkirk 6' coal; e) annotated hand specimen displaying the vein relationships**
194 **present during the faulting of the Muirkirk 6' coal; and f) the larger-scale mineralisation pattern**
195 **as you move towards small stratigraphic separation faults in the Muirkirk 6' coal.**

196 Fractures at Spireslack SCM can be classified as either joints (barren open mode fractures), faulted
197 joints (joints that show evidence of reactivation, E.g., mineralisation or cataclasis) , or shear fractures,
198 with the latter two often found in proximity to faults. In this study ‘shear fractures’ refer to a fracture
199 with displacement below map scale and can be either mineralised or barren. Crosscutting relationships
200 are often complex and display several age sets. For example, in the McDonald Limestone bedding plane
201 (Figure 3a) there are two generations of joints: an early set of NE-SW trending joints (dashed black in
202 Figure 3a) and a later set of N-S trending joints (black) that abut the earlier set. Both generations
203 represent the pre-existing fracture set at the time of faulting. These pre-existing joints are then cut by a
204 set of NNE-SSW trending mineralised shear fractures (dashed blue) that are restricted by favourably
205 orientated joints and are locally are associated with new barren shear fractures (lilac). Finally, several of
206 the N-S trending joints become reactivated (maroon) and are interpreted as faulted joints (c. Zhao and
207 Johnson, 1992).

208 Calcite mineralisation at Spireslack SCM (Figure 3b, c), which is often found associated with faults,
209 occurs as two styles: 1) amorphous, where no growth structures are present and occasional fragments of
210 limestone are observed within the vein, or 2) with syntaxial growth textures suggesting both sinistral
211 and dextral motion during the mineralisation of a single vein (Figure 3c). Along fault planes and within
212 a few meters of faults, composite veins commonly occur, with multiple growth stages and evidence of
213 reactivation (Figure 3c).

214 Fractures in the coal layers are commonly filled with a buff to orange coloured mineral, identified in the
215 field as ankerite (iron rich carbonate) (Figure 3d-f). Fractures in coal occur as:

216 - *Coal cleats*: Ubiquitous in all coals, cleats are orthogonal opening mode fractures that develop
217 during burial diagenesis (Laubach et al., 1998). Cleat spacing (typically <2 cm) is dependent on
218 bed-thickness, coal quality and the presence of clastic material (e.g. shale partings).
219 - *Mineralised shear fractures*: Typically 2 to 15 cm long, but increase to greater than 1 m long as
220 stratigraphic separation increases. Fractures less than 15 cm long abut against E-W trending

221 cleats, with trace length restricted by cleat spacing. Longer fractures cut through the cleats. The
222 thickness of planar ankerite veins increases with the length of the vein.

223 - *En-echelon arrays*: En-echelon ankerite veins display both sinistral and dextral motion (Figure
224 3d). Dextral arrays can occur both simultaneously with, or later than, sinistral arrays.

225 - *Barren shear fractures*: In addition to the cleat network, fractures that abut against all other
226 fractures are often curved and have trace lengths typically between 5 to 15 cm. These may
227 propagate from the tip of pre-existing mineralised shear fractures (Figure 3d).

228 Other lithologies observed in Spireslack SCM display a strongly developed fracture stratigraphy (c.f.
229 Laubach *et al.* (2009)). For example, the McDonald Seat Earth exposed in the dip-slope towards the
230 west of the site (Figure 4a), lacks a well-developed joint pattern. Instead, shear-fractures are observed in
231 relation to small stratigraphic offset, strike-slip faults (Figure 5a,b). Fractures are only found in close
232 proximity to fault strands and are either sub-parallel to fault strands in the hanging wall block, or
233 oblique to the fault strands in relay zones and fault tips. Fractures commonly display small sinistral and
234 dextral stratigraphic offsets (mm to cm) and are typically barren, although occasionally pyrite is found
235 along the fracture plane. Sandstones display bed-bound joint-sets in a similar manner to the McDonald
236 Limestone. However, there was limited bed-parallel exposure to explore the age and orientation of
237 fracture sets in sandstone lithologies. In contrast to the dip-slope, seat-earth in the high wall displays a
238 well-developed bed-bound fracture network. This suggests that mine-related stresses may have caused
239 deformation of these lithologies and that the natural network has been altered by both subsurface and
240 surface mining activities.

241 **4.1.1. Order of fractures within the Muirkirk 6' coal**

242 Like the McDonald Limestone bedding plane (Figure 3a-c), a complex chronology of fractures can be
243 observed in the Muirkirk 6' coal (Figure 3d-f). In Figure 3d, dextral en-echelon vein arrays (red)
244 crosscut earlier sinistral sets (blue), with the former abutting against mineralised shear fractures. Barren
245 shear fractures then abut against both sets displaying a curvature indicative of a dextral fracture array.
246 Abutting relationships suggest the barren shear fractures likely formed at the same time as the dextral
247 en-echelon vein array; however, given the lack of mineralisation it is likely they were isolated from the
248 source of mineral rich fluids.

249 In Figure 3e, multiple phases of mineralisation and reactivation of veins can be observed. Veinlets of
250 ankerite both abut against, and cut through, the calcite vein associated with a nearby small (<5 cm)
251 stratigraphic offset fault. Brecciation of coal and calcite is also observed, with undisrupted ankerite

252 veinlets cutting through the breccia. This requires a minimum of four stages of
253 mineralisation/deformation:

254 1) Ankerite veinlets formed along the N-S striking face-cleats.

255 2) Faulting led to the development of coal breccia and calcite veining which either cut across or
256 abut against pre-existing structures.

257 3) Brecciation of the calcite vein and coal led to the development of a chaotic fault breccia
258 (following the classification of Woodcock and Mort (2008)). The breccia contains angular clasts
259 of coal and calcite within an amorphous calcite matrix.

260 4) Finally, mineralisation returned to ankerite with dextral en-échelon arrays developed
261 alongside barren tip-damage zones.

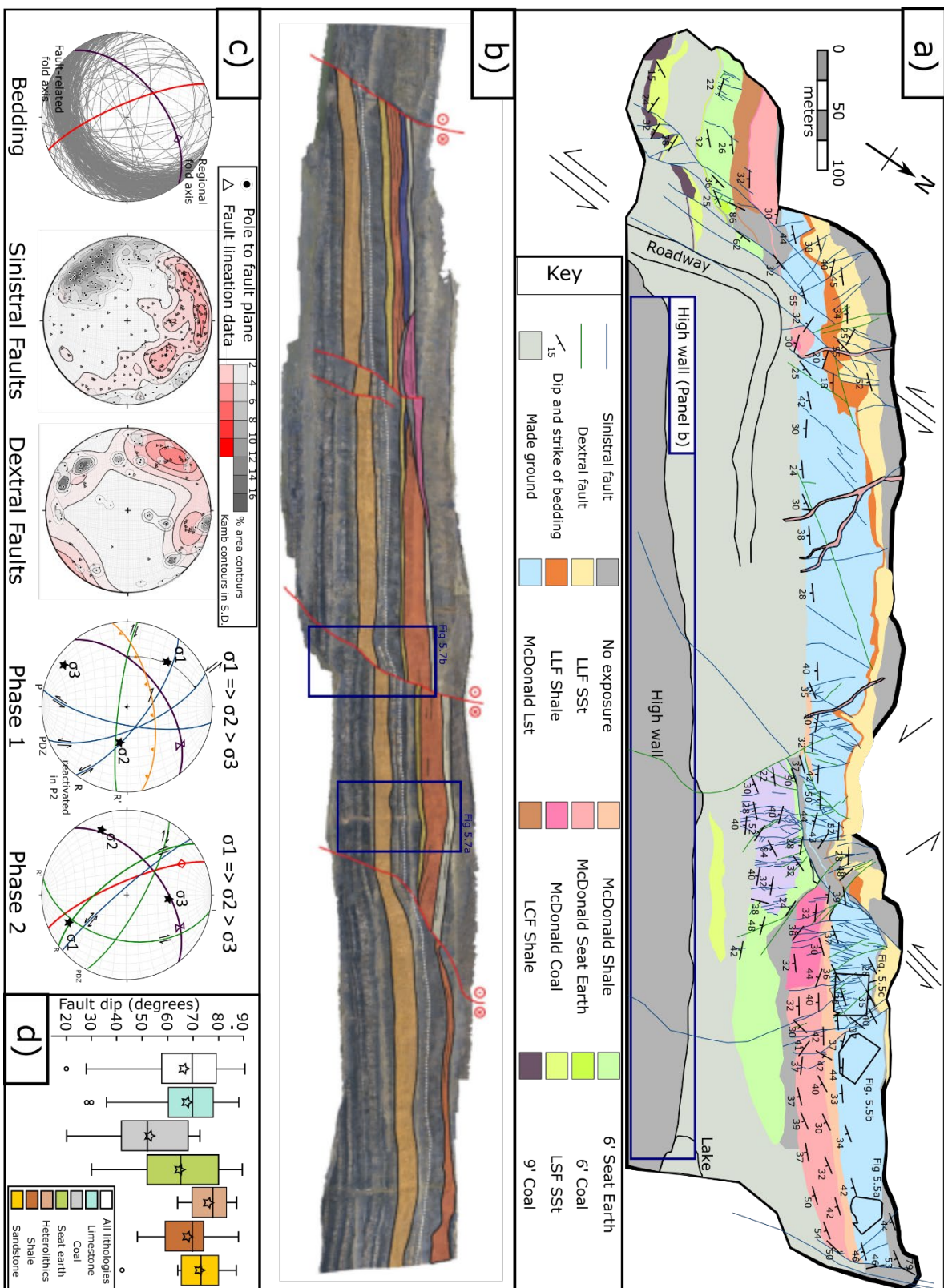
262 These observations suggest that initial deformation and associated mineralisation occurred over a wide
263 zone of en-échelon arrays (Figure 3d), which was strongly influenced by the pre-existing cleat network
264 (Figure 3e). En-échelon arrays then began to interact leading to the development of localised
265 mineralised shear fractures (Figure 3f). As the trace length of the shear fracture increased, so did the
266 thickness of the zone leading to the formation of a dense array of small stratigraphic offset (<1 cm)
267 strands which interacted through the development of relay-zones. A later dextral stress state,
268 demonstrated by reactivated features (Figure 3e), lead to another phase of en-echelon vein formation
269 (Figure 3c), which also locally developed into mineralised shear fractures.

270 **4.2 Fault observations**

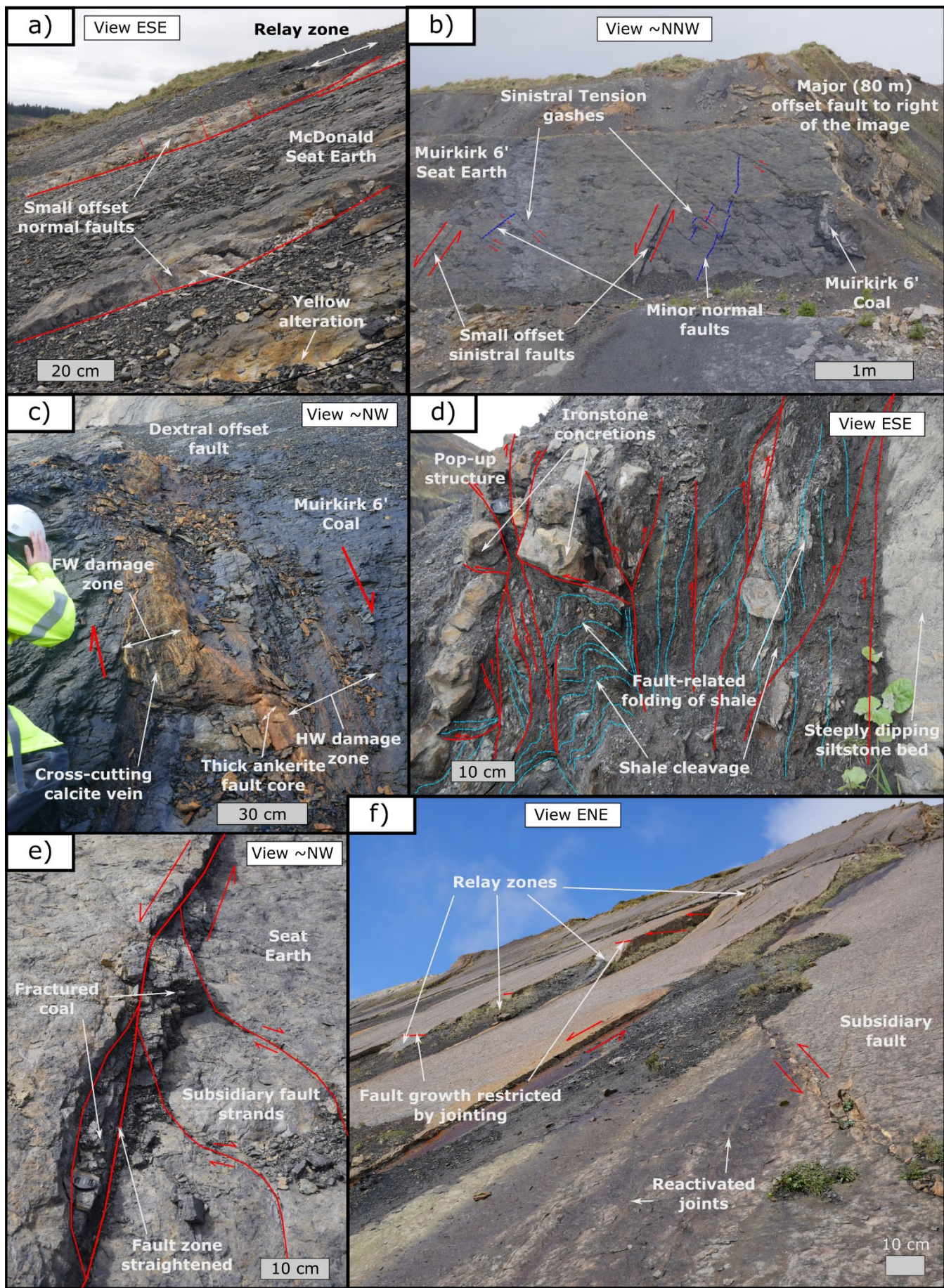
271 In order to understand the role of lithology on faulting style we describe and compare fault
272 characteristics between faults that cut the same lithology (self-juxtaposed faults) and faults that
273 juxtapose multiple lithologies of the stratified sequence. Additionally, in order to elucidate the role of
274 pre-existing joints on faulting style, we focus on the interaction between faults and fractures within the
275 McDonald Limestone formation because of exceptional, laterally extensive bed-parallel exposure on the
276 dip-slope.

277 The majority of faulting at Spireslack SCM fits into the expected fault geometries for Riedel shears
278 under a sinistral (Phase 1), or dextral (Phase 2) shear sense (Figure 4c). In this model, early dextral
279 faults represent R' Riedel shears and formed concurrently with normal faults in the 6' Seat Earth and
280 thrusts in the shale. The south-dipping bedding, is consistent with the regional fold axis inferred from

281 BGS maps (040°/80° N) also fits within the sinistral phase of deformation. Faulting that cuts the earlier
282 structures (e.g. the oblique sinistral fault and NW trending dextral fault strands) does not fit within the
283 expected fault geometries of Phase 1 faults, and likely formed under a later period of dextral shear
284 (Phase 2) (Figure 4c). In addition to the two phases of strike-slip tectonics, dykes (probably Paleogene)
285 exploit pre-existing N-W trending fault strands. These locally display pods of edge brecciation similar
286 to that developed along faults in limestone, and show dip-slip lineations suggesting there could have
287 been a late stage of normal faulting.



290 **Figure 4: Geological map of Spireslack SCM: a) geological map undertaken as part of this study,**
 291 **displaying the locations of the detailed map-view fracture maps shown in Figure 8; b) annotated**
 292 **photogrammetry of the high wall displaying the key stratigraphic horizons and faults (Ellen et al.,**
 293 **2019); c) fault kinematics by lithology. Stereographic projections were created using Stereonet**
 294 **10.1 and contours represent 1% area; and d) box and whisker plots for fault dip by lithology.**



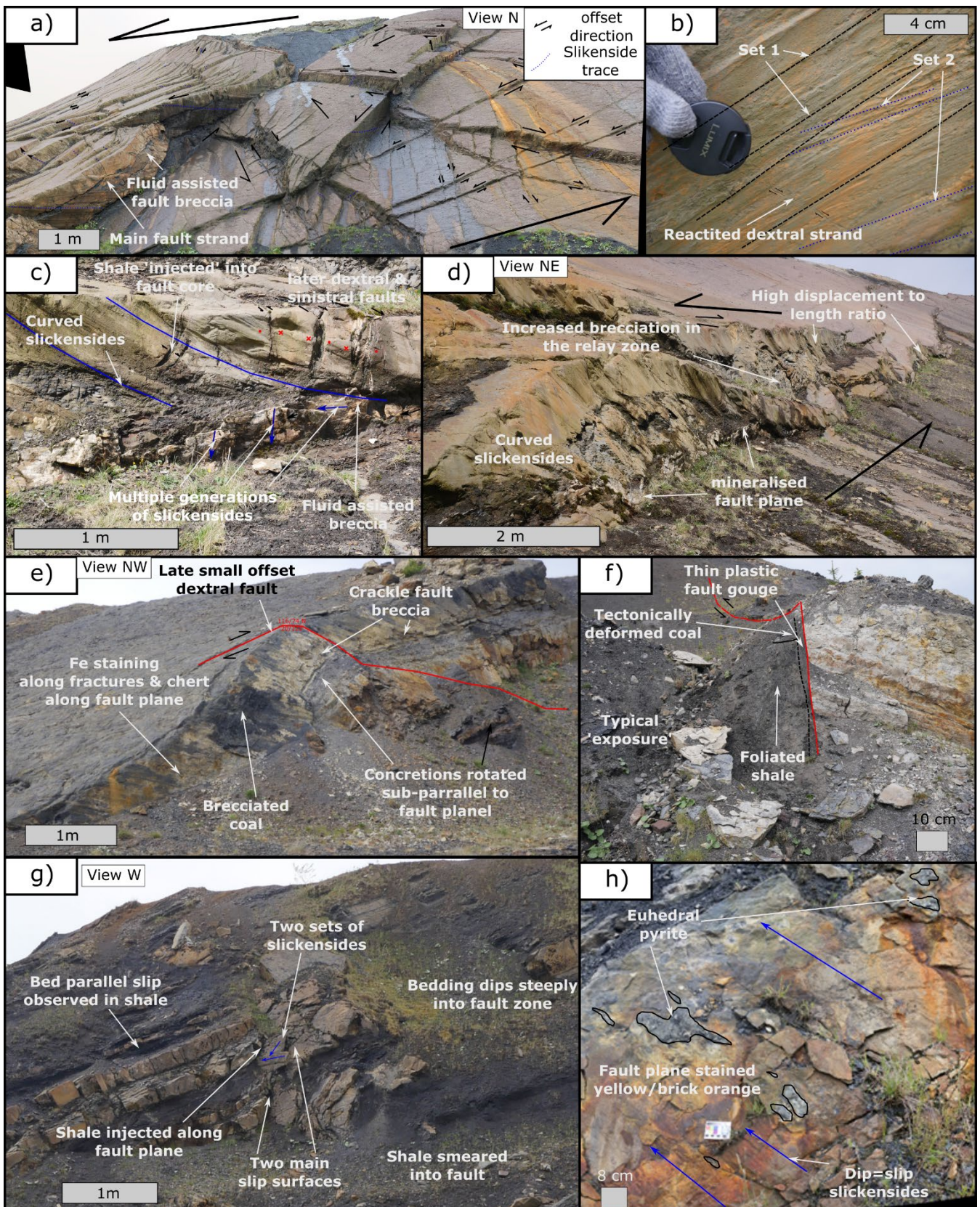
296 **Figure 5: Characteristic observations of Self Juxtaposed Faults (SJFs): a) Small stratigraphic offset (c.
297 15 cm) fault strands and relay structures, and b) tension gashes and small stratigraphic offset normal
298 faults exposed within the McDonald Seat Earth in seat-earth exposed to the far west of Spireslack
299 SCM; c) symmetric damage zone and thick zone of ankerite mineralisation along a c. 40 cm
300 stratigraphic separation dextral fault cutting the Muirkirk 6' Coal [FW = Footwall, HW = Hanging
301 wall]; d) bed-parallel thrusts and folding developed within the shale which underlies the McDonald
302 Limestone to the NE of the site; e) the development of small pods of fractured McDonald Coal along
303 a small stratigraphic offset sinistral fault exposed to the SW of the site; f) the interaction between
304 faults and joints along the southerly dipping bedding plane of the McDonald Limestone.**

305 Self-juxtaposed faults, with small stratigraphic offset (<3 m), form either isolated strands (e.g. west of
306 the void) or a network of sinistral and dextral strands (e.g. near the centre of the void) (Figure 3). The
307 internal structure of self-juxtaposed faults depends on the lithology that the fault strand cuts (Table 1,
308 Figure 4). Self-juxtaposed limestones behave in a predominantly brittle manner with a fracture network
309 decreasing in intensity away from the fault. Whereas, shale behaves in a more ductile manner and can
310 lead to considerable bed-rotation and bed-parallel folding adjacent to the fault.

311 The fault dip depends on the lithology cut by the fault. Dips in the McDonald Limestone range from 45°
312 to 88° (mean = 69.1°, n = 47), however, in coal seams fault dips range from 20° to 73° (mean = 49°, n =
313 24). In the shale interbeds, layer bound, bed-parallel thrusts (e.g. 040°/70° SE) with cm- to m-scale
314 stratigraphic offsets and associated folding can be picked out where they cut ironstone layers (Figure
315 5d). The McDonald Seat Earth in the west of the site displays dip-slip slickensides (50° to 60°), but only
316 in faults with stratigraphic separation <1 m.

Lithology	Self-juxtaposed fault characteristics
McDonald Seat Earth	Segment linkage, folding, and increased fracturing between strands led to the development of a highly asymmetric damage zone (Figure 5a, b, e). Faults typically barren, only displaying yellow alteration and occasionally pyrite.
McDonald Limestone	Self-juxtaposed faults, associated relay zones, and nearby N-S trending joint sets, are mineralised (calcite), display high displacement to length ratios (2.4 to 2.8), and show extensive folding of the surrounding lithologies (Figure 5f). Strands often abut against favourably orientated pre-existing joints.
Coal	Fault strands are characterised by a fault core comprising of a 5 to 20 cm thick zone of ankerite, with occasional calcite mineralisation, brecciated coal and pyrite (Figure 5c). The fault core is discontinuous along strike, with displacement transferring to other strands after 1 to 5 meters (Figure 5c). The gentle folding of the bed between strands is taken up by a symmetric zone of damage consisting of increased fracturing, en-echelon veining and mineralised shear fractures. The structures represent a continuation of the processes discussed in Section 4.1.1.
Shale	Fault strands are rarely observed. High angle thrusts (40° to 60°) dominate, with bed parallel folding picked out by ironstone concretions (Figure 5d), which themselves can display internal deformation (tension gashes). Near self-juxtaposed faults a cleavage is developed sub-parallel to the fault plane, which combined with slickenfibers on competent bedding planes suggests bed-parallel slip.

317 **Table 1: Self Juxtaposed Fault characteristics by lithology.**



320 **Figure 6: Characteristics of faults that cut multiple lithologies: a) complex fault mesh (after**
 321 **Sibson, (1996)) consisting of multiple strands of sinistral and dextral strike-slip fault planes**
 322 **(stratigraphic separation marked with arrows) picked out by shallow striations and the offset of**
 323 **the McDonald Limestone bedding plane; b) field photograph of a ~3 m stratigraphic separation**

324 **fault strand within the complex fault mesh (a) which displays multiple generations of fault**
325 **striations, with local dextral reactivation separating striations belonging to set 2; c) fault**
326 **architecture and d) view along a ~50 m strike-length of a highly segmented fault zone displaying**
327 **3 to 5 m stratigraphic separation exposed along the southerly dipping bedding dip-slope; fault**
328 **architecture of the same 5 m stratigraphic separation fault cutting e) lithologies surrounding the**
329 **McDonald Seat Earth, and g) interbedded sandstones, siltstones and shales of the Lower**
330 **Limestone Coal Formation; f) primary slip plane of the ~80 m stratigraphic separation fault**
331 **which cuts the west of the site; and h) shallowly dipping, sinistral dip-slip fault plane within a ~2**
332 **m thick sandstone bed of the Limestone Coal Formation.**

333 Key features observed along faults that juxtapose multiple lithologies (i.e. that are non self-juxtaposed)
334 are summarised in Table 2. Based on cross-cutting relationships we observe two phases of faulting at
335 Spireslack SCM.

336 Larger stratigraphic offset (>5 m) faults that cut multiple lithologies display complex deformation styles
337 (Figure 6, 7; Table 2) that depend on: a) the lithologies cut by the fault; b) the plane of observation (i.e.
338 map (Figure 4) vs high wall (Figure 7)); and the phase of faulting (Figures 4, 5 & 6). Fault dips vary
339 considerably between different lithologies, with steeper dips observed in competent lithologies (Figure
340 4d), as well as varying down dip along a single fault plane (Figure 6e, g; Table 2). Variations in fault
341 dip causes bed rotation and the development of fault-core lenses consisting of sandstone and seat earth
342 that are elongated parallel to fault strike lenses (Figure 4a, 6). Bedding is folded towards the faults
343 (Figure 4 & 6), with folding more intense in interbedded lithologies (Figure 6g, 7) and shale (Figure 6f).
344 The majority of throw on faults with over 5 m stratigraphic separation is accommodated along one
345 (Figures 6b, c & 7a) or two (Fig. 7b) principal slip zones. Principal slip zones, particularly for Phase 1
346 faults, are typically straight and steep (>70°) (Figures 6 & 7) and are surrounded by a variably thick
347 damage zone of shear fractures and self-juxtaposed faults (Figure 7), with thickness that varies between
348 lithologies.

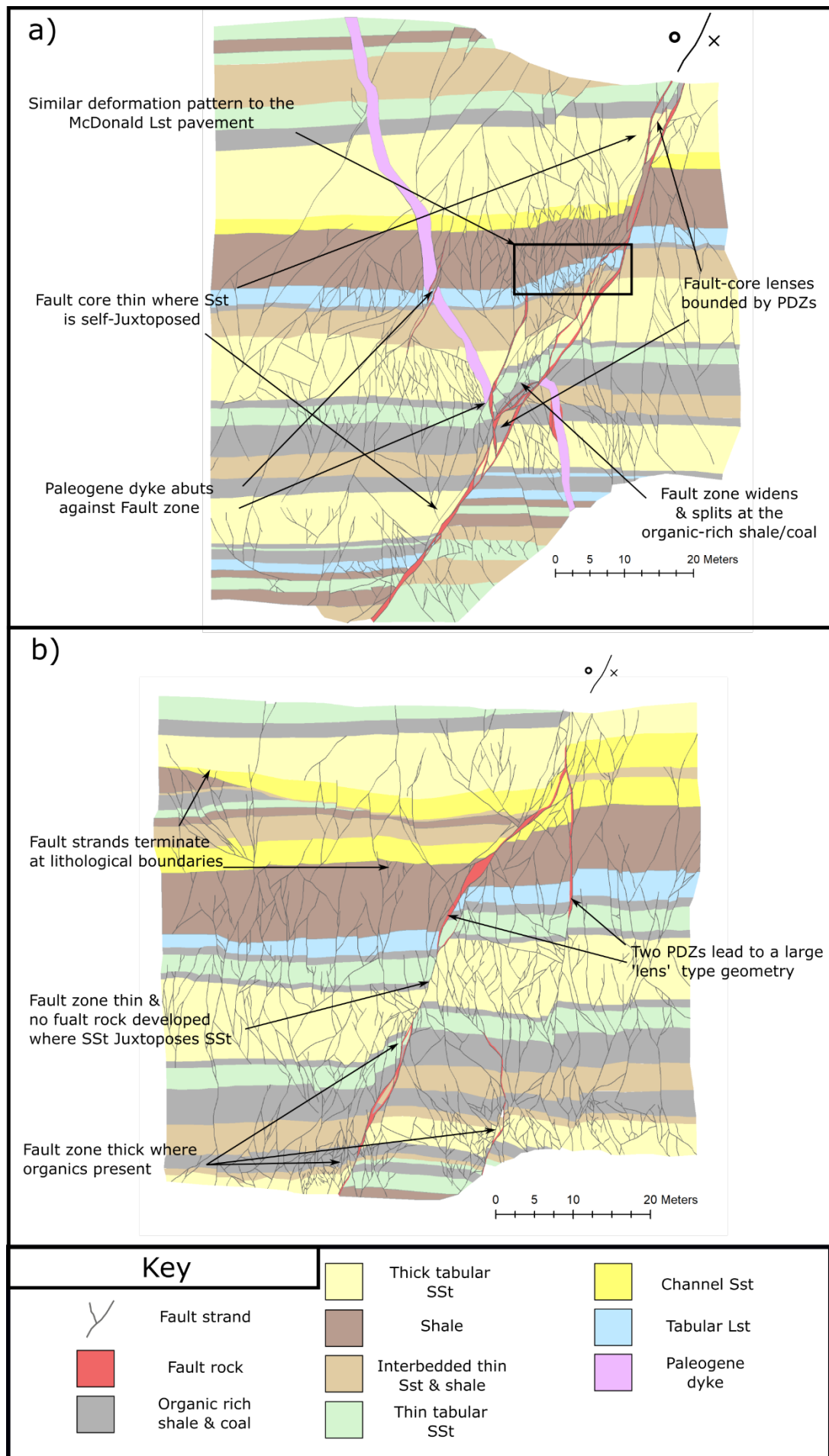
349 Fault core thickness is typically low (<5 cm) and displays a highly variable internal structure both along
350 strike and down dip (Table 2, Figure 7). All faults display strike-parallel corrugations (Figure 6d, e, h)
351 that often display brecciated coal (Figure 6e). Phase 1 faults are often mineralised with calcite (Figure
352 6c), display multiple slip events (Figure 6c), and locally display evidence of shale injected along the
353 fault plane (Table 2). Conversely, Phase 2 faults rarely display calcite mineralisation and instead show
354 evidence of syn-tectonic pyrite mineralisation (Figure 6h). Where Phase 1 and 2 faults interact, for
355 example in the centre of the void (Figure 4a), a complex fault mesh is developed with displacement
356 distributed over several sinistral and dextral fault strands (Figures 3 & 6a, b).

Fault (fault phase)	Stratigraphic separation	Lithologies cut	Fig(s)	Key Features
Fault meshes in the McDonald Lst. and LLF (Phase 1 & 2)	<3 m	Limestone, shale, locally siltstone	6a, 6b	<ul style="list-style-type: none"> Bedding strongly rotated and tension gashes developed. Fault cores are mineralized and thin (<5 cm) across all displacements. Slickenfibers are curved and record multiple generations of fault slip.
Mineralised sinistral fault cutting the McDonald Lst	3 to 5 m	Limestone, shale	6c, 6d	<ul style="list-style-type: none"> Fault planes mineralized and several have high displacement to length ratios. Slickenfibers are curved and record multiple generations of fault slip. Fluid assisted breccia, particularly in relay zones. Phase 1 faults cut by Phase 2 faults. Shale injected into fault core.
Dip-slip faulting of sandstones and seat earths (Phase 2)	3 to 5 m	Decimeter bedded seat-earth, sandstones and shale.	6h	<ul style="list-style-type: none"> Shallowly dipping fault plane with dip-slip lineations. Fault plane displays alteration and syn-kinematic euhedral pyrite. Brecciated and friable coal present in the fault core.
Fault cutting interbedded lithologies. (Phase 1)	~5 m	Limestones, sandstones, seat-earth.	6b, 6c	<ul style="list-style-type: none"> In seat earth fault dip changes from ~60° near the base of the outcrop to 79° near the top. Brecciated coal is found within undulations on the fault plane. Bedding in both Fig. 6b and 6c displays folding with wavelength decreasing and dip increasing towards the fault. In the LLF a 2 to 3 m thick, mineralized fault zone is developed that displays multiple slip events. Shale appears to have been locally injected into mineralized fractures.
Large fault cutting the whole sequence (Phase 1)	80 to 100 m	Interbedded lithologies of the LCF and LLF	6e	<ul style="list-style-type: none"> Footwall damage zone consists of a highly fractured seat earth, with highly folded shale and altered coal in the hanging wall. The fault core consists of a thin (<5 cm) fault gouge containing clasts of sandstone and organic fragments.
High wall, faults (Phase 1)	Fig 7a = 10 to 12 m Fig 7b = 6 to 10 m	Interbedded lithologies of the LCF and Spireslack Sandstone	7a, 7b	<ul style="list-style-type: none"> The majority of throw is taken up by a small number of steep fault strands. Fault-core thickness is typically thin (<5 cm) and highly variable down dip. Fault-core lenses locally developed, particularly in interbedded units. Damage zones vary in thickness depending on lithology and consist of an interconnected network of self-juxtaposed faults and shear fractures.

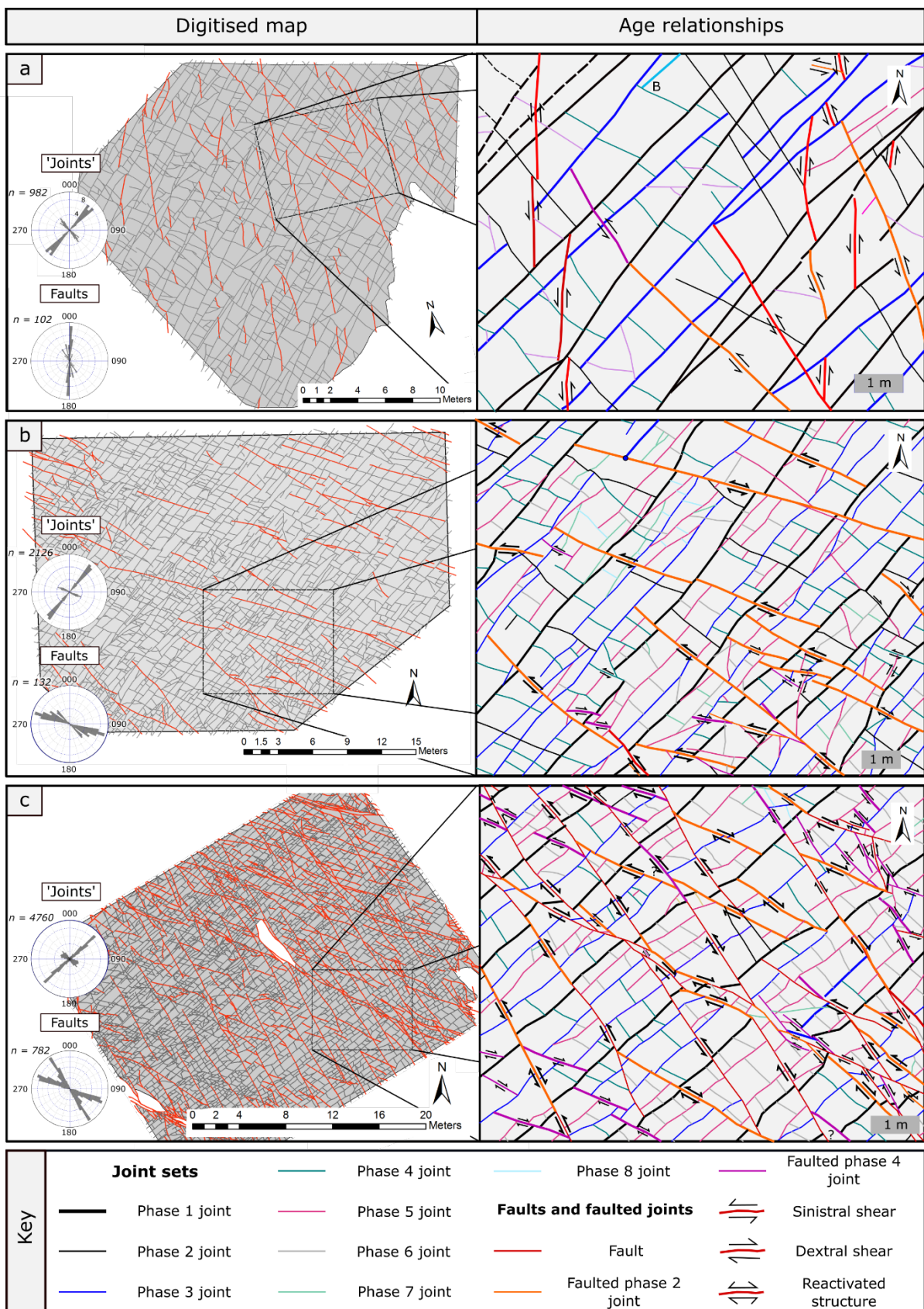
357 **Table 2: Summary of the key features observed along faults that juxtapose multiple lithologies.**

358 Please see S3 for full field descriptions. LLF = Lower Limestone Formation, LCF = Limestone

359 Coal Formation.



361 **Figure 7: Digitised fault strands of sinistral faults cutting the Limestone Coal Formation exposed**
362 **along the high wall: a) sinistral fault which displays between 2 and 5 m of apparent (vertical)**
363 **throw and has been cut by a later Paleogene dyke which is not observed within the fault core; b)**
364 **sinistral fault with displays between 2 and 8 m apparent (vertical) throw along two principle**
365 **displacement zones (PDZs). SSt = sandstone, Lst = Limestone. Photomontage provided courtesy**
366 **of the British Geological Survey (BGS).**



369 **Figure 8 Fracture maps with increasing intensity of faulting:** For each digitised map the exported
 370 fault (red lines) and 'joint' (dark grey lines) maps, along with the interpretation areas used for the
 371 analysis (light grey) are provided.

372 The style of the fault and fracture network in the McDonald Limestone changes across the site (Figure
373 8) with the chronology and network properties of each sample area described below. In this section
374 mineralised shear fractures, which are often faulted joints, are classified as faults for the network
375 analysis.

376 ***Fracture relationships at low fault intensity:***

377 The interpretation area in Figure 8a is dominated by large trace-length, NE trending, joints and smaller
378 trace length NNW trending joints. Abutting relationships suggest these formed as four distinct phases,
379 with two phases occurring at each orientation. The fault network displays two orientation sets (N and
380 NNW) of sinistral faults with low connectivity, trace length, and intensity (Table 3). Both fault sets
381 abut against favourably orientated Phase 1 or Phase 3 joints, indicating they formed later. Abutting
382 relationships of Phase 3 joints against NNW trending faults suggesting Phase 2 joints were reactivated
383 as faulted joints (after Zhao and Johnson, 1992) during the first phase of faulting. Phase 5 and 6 joints,
384 that display variable orientations in Figure 8a, abut against the faults suggesting they formed later.

385 ***Fracture relationships where joints are favourably orientated for reactivation:***

386 The interpretation area in Figure 8b, which is located slightly closer to the NW trending dextral fault
387 zone that cuts the middle of the site (Figure 4), displays a similar intensity of faulting ($I = 0.5 \text{ f/m}$),
388 however, joint intensity is higher ($I = 2.8 \text{ f/m}$). Joints from Phases 1 to 4 are observed in this panel;
389 however, faulting caused the segmentation of NNW trending Phase 1 and 3 joints such that the recorded
390 trace length of these joints in this panel is decreased compared to Figure 8a. Unlike Figure 8a, where
391 only sinistral faults were observed, both sinistral and dextral offsets are present in Figure 8b. Fault
392 orientations were typically either ENE or NE with the number of northerly faults significantly decreased
393 (Table 3). Abutting relationships of faults in this panel suggests that the majority of strands represent
394 reactivated Phase 2 (orange) or Phase 4 (purple) joints. The majority of faulted Phase 2 joints display
395 sinistral offset or evidence of reactivation, while Phase 4 joints display predominantly dextral offsets.
396 Abutting relationships suggest that faulting occurred as two phases, with joint development occurring
397 both between (Phase 5 and 6) and following (Phase 7 and 8) the formation of dextral faults.

398 ***Fracture relationships where both phases of faulting is present***

399 The interpretation area in Figure 8c is located close to the major NW-trending dextral fault (Figure 4),
400 and includes two self-juxtaposed faults towards the bottom and top of the studied section (Figure 8c).
401 The panel displays a complex fracture evolution, however, many of the features observed in the

402 previous panels are visible. Phase 1 to 4 joints are still easily identified; however, their trace length has
403 further decreased due to increased fault intensity ($I = 1.9$ f/m). Unlike figures 8a and 8b, the fault
404 network is well connected in this panel ($P_c = 0.71$), with individual fault strands linking to form locally
405 complex relay zones (e.g. the bottom left of Figure 8c). Abundant sinistral, dextral, and reactivated fault
406 strands are observed, with Phase 2 and 4 joints regularly becoming reactivated and linked by new fault
407 strands. Locally, Phase 6 joints are also reactivated in a dextral sense (e.g., the relay zone in the NE of
408 Figure 8c). The number of joints that abut against faults and the pre-existing joint sets (Phase 1 to 4) is
409 greatly increased in this panel, with several Phase 7 and 8 joints identified.

410 ***Summary of structures***

411 As fault intensity increases, the complexity of age relationships in the fault-fracture network also
412 increases (Figure 8). Phase 1 to 4 joints are identified across all three panels and are interpreted as the
413 ‘pre-existing’ joint network. As fault intensity increases, these ‘pre-existing’ features become
414 segmented through faulting and their recorded trace length decreases. While fault intensity is similar in
415 Figure 8a and 8b, faults with a N-S strike are only present in Fig 8a. This is probably due to the subtle
416 anticlockwise rotation of the pre-existing joints relative to the stress field that enabled the reactivation
417 of Phase 2 and 4 as faulted joints (Figure 8b, c) and promoted the formation of Phase 5 and 6 joints
418 (orange and purple lines in Figure 8). The number of faulted joints drastically increases with increased
419 fault intensity, with joints becoming linked through the formation of new fault strands. In agreement
420 with the void-scale mapping (Figure 4), two phases of faulting have been identified in Figure 8b and 8c,
421 with an earlier sinistral and later dextral phase. The sinistral phase appears to preferentially reactivate
422 Phase 2 joints whereas the dextral phase preferentially reactivated both Phase 2 and 4 joints. The
423 increase in reactivated joints, and two clear phases of faulting in Figure 8c explains the large increase in
424 joint intensity in this panel ($I = 4$ f/m compared to $I = 2.6$ f/m in Figure 8a). While age relationships are
425 reasonably consistent across this section of the limestone pavement, as fault-meshes begin to form, age
426 relationships become increasingly complex and spatially variable (Figure 6a). This suggests a highly
427 heterogeneous stress field, which was rotated relative to locally active fault strands. An increase in fault
428 throw also affects the intensity, trace-length and connectivity of the network.

Sample area	Key features	‘ Joint’	% of nodes				Pc	Sets	# fr	Tl (m)			I (f/m)						
			I	Y	X	E				Min	Max	Med.							
1 Fig. 5a	Faults are mineralized and display syntaxis crack seal growth textures.	‘ Joint’	13	72	46	5	0.95	0	132	0.23	10.78	1.29	0.5						
								1	72	0.10	10.43	1.02	0.3						
								2	400	0.09	14.71	0.93	1.5						
								3	78	0.15	9.89	0.95	0.3						
		Faults	83	19	0	14	0.24	0	1	0.22	9.33	1.62	-						
								1	0	-	-	3.82	-						
								2	15	-	-	-	0.1						
								3	86	0.73	7.44	1.37	0.4						
2 Fig. 5b	SA2 is dominated by barren joints and shear fractures, with faults reactivating favorably orientated pre-existing joints.	‘ Joints’	24	85	20	3	0.90	0	789	0.02	10.33	1.32	1.7						
								1	171	0.10	4.18	0.70	0.2						
								2	561	0.09	6.93	0.79	0.7						
								3	412	0.09	4.44	0.59	0.4						
		Faults	80	26	0	20	0.28	4	193	0.09	4.14	0.59	0.2						
								0	-	-	-	-	-						
								1	3	0.90	1.38	1.16	0.0						
								2	24	0.47	13.16	2.43	0.3						
		‘ Joints’	46	48	3	2	0.77	3	53	0.78	8.66	2.53	0.2						
								4	19	0.21	3.16	1.74	0.0						
3 Fig. 5c	The fault and fracture network is highly variable in SA3, with complex relationships between pre-existing joints, faulted joints, faults, and fracture corridors.							0	2000	0.04	5.49	0.74	2.4						
								1	464	0.06	2.97	0.39	0.3						
								2	903	0.05	2.86	0.38	0.5						
								3	1056	0.05	3.09	0.35	0.6						
								4	355	0.05	1.90	0.28	0.2						
	Faults	49	66	1	13	0.71	0	0.04	5.49	0.74	0.04	2.4							
							1	0.06	2.97	0.39	0.06	0.3							
							2	0.05	2.86	0.38	0.05	0.5							
							3	0.05	3.09	0.35	0.05	0.6							
							4	0.05	1.90	0.28	0.05	0.2							

429 **Table 3 Network characteristics of the joint and fault datasets presented for the three sample**
430 **areas outlined in Figure 8. For the combined network fracture statistics, and trace length**
431 **distributions for all datasets please refer to S2.**

432 **5. Structural Evolution at Spireslack SCM**

433 The exceptional 3D exposures of the Limestone Coal Formation and surrounding lithologies have
434 informed a 5-stage conceptual model for the development of the structures (Table 4). While this model
435 is based on observations from the Spireslack SCM void, the model could be improved by utilising data
436 from nearby open cast sites (Leslie et al., 2016), legacy subsurface data as introduced in Ellen et al.
437 (2016), and additional correlation with the larger scale structures observed in the Midland Valley of
438 Scotland.

Timing	Stage/regional	Faulting and folding	The whole sequence	McDonald Limestone	Muirkirk 6' Coal
Stage 1: Initial sedimentation and burial	Extensional reactivation of Caledonian lineaments led to NE-SE ^{1,2} or EW ³ orientated back-arc extension and rapid rift development ^{1,2} .	Although deposition was influence by fault movement (e.g. Spireslack Sandstone ⁴), no evidence of early (Dinantian) extensional faults, that are common across the Midland Valley ^{5,6} , are observed at Spireslack SCM.	During the Carboniferous the Midland Valley was located close to the equator ⁷ , with sedimentation dominated by a coal bearing fluvio-deltaic depositional system ^{8,9} .	Occasional marine incursions, caused by eustatic and tectonics controls, led to the deposition of regionally extensive marine limestones (e.g. the McDonald Limestones) ¹⁰ .	Peat swamps, that formed on swampy delta tops ¹¹ , were converted to coal during the process of coalification ¹² . This causes cleats to form, with cleat orientation suggesting a NS orientated maximum compressive stress ¹³ .
	Folding in Ayrshire is attributed to late Visean syn-depositional compression ² .	Bedding became folded towards the SE, with the early influence of sinistral wrench tectonics (stage 2) possibly causing some NS orientated folds to develop (Fig. 3c).	Bed-parallel shear in shale (Fig 4d) was associated with regional folding and probably continued into Stage 2.	A series of barren, sparsely spaced joints formed (Phase 1 & 2 joints) (Fig. 5), prior to being slightly rotated prior to the formation of Phase 3 & 4 joints. Joint Phases 1-4 represent the pre-faulting fracture state (Fig. 5a).	Early ankerite mineralization of N-trending face cleats (Fig. 2d-f).
Stage 2: Sinistral transpression	Sinistral transpression widely effected the Midland Valley during the mid-to-late Carboniferous ^{2, 14} , with structures at Spireslack SCM having been previously attributed to this stage ¹⁵ .	Formation of sinistral offset faults with shallow lineations (Fig 3c) was accompanied by associated minor dextral faulting (Phase 1; Fig 3a, c) and local fault-related folds (Fig 6). Faults typically display mineralization (Figs 2, 4 & 6), with evidence of multiple crack-seal events (Fig 2c, e).	Because of multiple pre-existing joint sets and a well-developed mechanical stratigraphy, trace length of individual fault strands is low and strain is taken up by several small faults.	Joint sets 1 and 3 restricted the growth of Phase 1 faults and favorably orientated Phase 2 joints were reactivated. Calcite mineralization commonly observed (Figs 4, 6) with evidence of multiple crack seal events (Fig. 2c). Joint sets 5 and 6 formed between Phase 1 and Phase 2 faults (Fig. 5b, c).	Sinistral en-échelon vein arrays and minor mineralized (Ankerite) shear fractures form (Fig. 2d, f). Faulting lead to the development of coal breccia and calcite veining which either cut across or abut against pre-existing structures (Fig. 2d-f)
Stage 3: Dextral transpression	Reversal in the shear direction during the Upper Carboniferous led to a period of Dextral transpression ^{14, 16, 2} .	NW trending dextral faults formed (Phase 2 faults) (Fig 3a, c), with associated reactivation of Phase 1 faults and pre-existing structures (Fig. 5). Phase 2 fault zones display syn-kinematic pyrite (Fig. 6h).	Fault-zones became well connected through the linkage of through-going faults (Fig 5c). Where Phase 1 and 2 faults interact, complex fault meshes developed (Fig 3a, 6a).	Joint sets 1 & 3 restricted the growth of Phase 2 faults, with joint sets 2, 4, and locally 6 being reactivated (Fig 5, b, c). Linking faults are preferentially orientated between 060° and 100° (Figs. 5c & 8) and joint sets 7 & 8 formed following Phase 2 faults (Fig 5b, c).	Reactivation of cleats and stage 2 features was accompanied by a further phase of ankerite mineralization, and local kink-band development (Fig 2 d-f).
Stage 4: Paleogene intrusions.	Basaltic dykes were intruded, with the orientation suggesting it is associated with the British Tertiary Igneous Province ¹⁷ .	No fragments of dyke are observed within the fault core in Fig 7a. This suggests the dyke broke through the fault core out of the plane of observation, as the dyke post-dates faulting.	Dyke orientation traced along the trend Phase 1 and 2 faults (Fig. 3).	Although not visible in the Muirkirk 6' coal, in the high wall the Muirkirk 9' coal becomes altered to white trap, a common trend in the Western Ayrshire Coalfield ¹⁸ .	

Stage 5: Post- Paleogene reactivation	NW-SE and locally NE-SW trending structures were reactivated, possibly associated with isostatic rebound or the opening of the North or Irish Seas.	No evidence of extensional reactivation is observed other than along the edge of the dyke.	Brecciation of the edge of the major dyke and surrounding limestones was coupled with dip-slip reactivation, suggesting post-intrusion extensional reactivation occurred.	No evidence of late stage reactivation observed.
---------------------------------------	---	--	---	--

439 **Table 4: Summary of the structural features observed at Spireslack SCM. References in the table:**
440 1) Leeder (1982); 2) Underhill et al. (2008); 3) Haszeldine (1984); 4) Ellen et al. (2019); 5) Coward,
441 (1993); 6) Anderson (1951); 7) Soper et al. (1992); 8) Browne et al. (1999); 9) Read et al., (2002);
442 10) George, (1978); 11) Thomas (2013); 12) O'Keefe et al. (2013); 13) Rippon et al. (2006); 14)
443 Ritchie et al. (2003); 15) Leslie et al., (2016); 16) Caldwell and Young (2013); 17) Emeleus and
444 Gyopari (1992); 18) Mykura (1965).

445 **6. Discussion**

446 **6.1 The effect pre-existing joints and coal cleats on subsequent deformation and network**
447 **connectivity**

448 The mechanically stratified succession at Spireslack SCM has led to the development of a fracture
449 stratigraphy (Laubach et al., 2009). While joints across the site locally display two ‘orientation sets’
450 (Figure 8, insets), abutting relationships discussed in section 4.4.3 identified 8 ‘age sets’ punctuated by
451 two phases of faulted joints (Figure 8). Different ‘orientation sets’ have previously been attributed to
452 separate tectonic events (e.g. Peacock et al., 2018; Sanderson, 2015) or situations where the
453 intermediate (σ_2) and minimum (σ_3) principal stresses are nearly identical, and can therefore easily
454 switch between each other (Caputo, 1995; Caputo and Hancock, 1998). It is likely the latter that
455 contributes to the rapid switching between ~NNW (Phase 1, 3, 5, & 7) and ~NE (Phase 2, 4, 6, & 8)
456 trending joint sets observed in Figure 8.

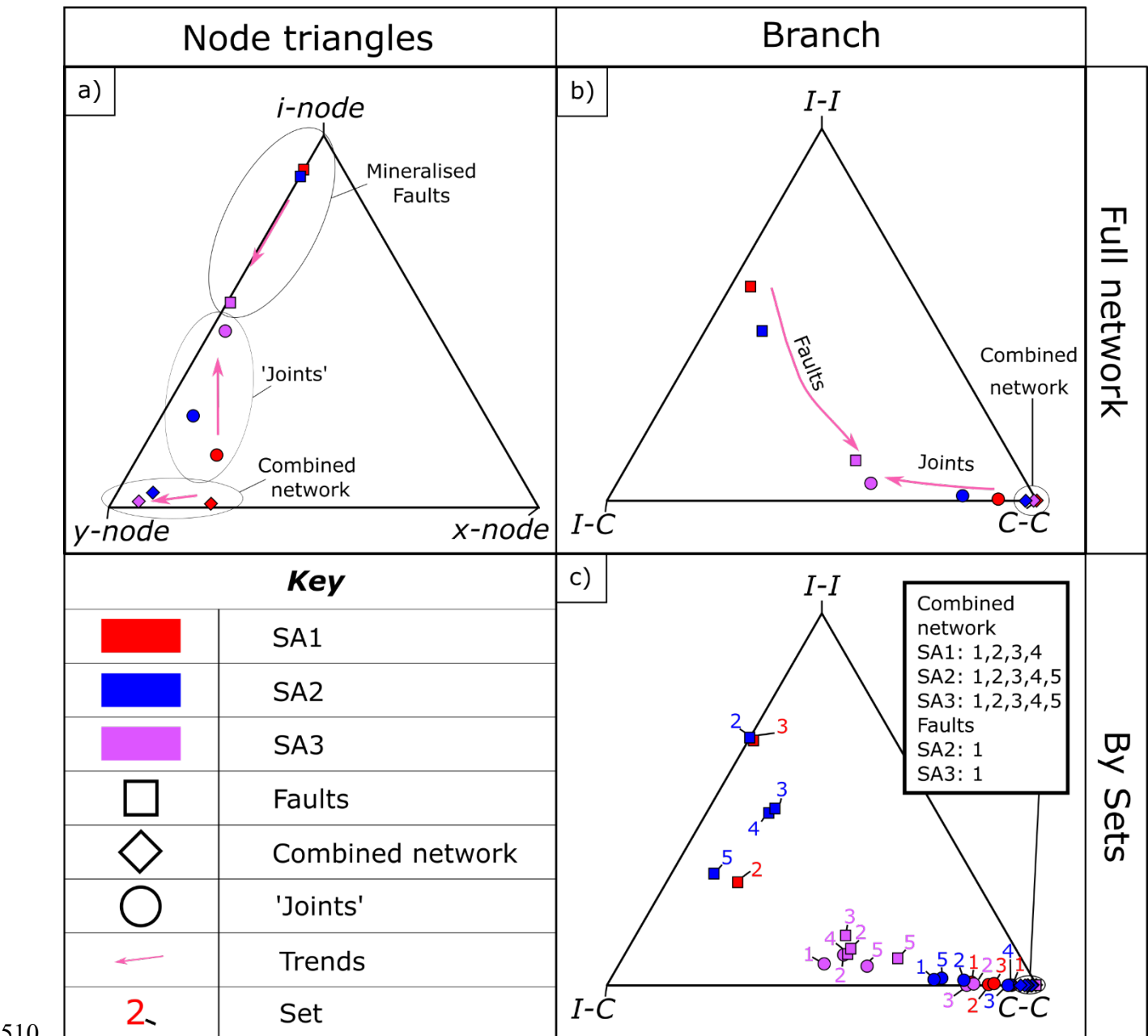
457 There are several examples of joints or cleats influencing fault growth at Spireslack SCM (Figure 3, 5,
458 8). Jones and Tanner (1995) found that transpressional strain can often become partitioned across pre-
459 existing structures. At Spireslack, joints appear to be accommodating the shear-strain component, with
460 pure-shear accommodated through the tightening of the Muirkirk Syncline. Throughout both
461 deformation phases, faults abutted against NE trending joint sets. However, during the sinistral phase of
462 faulting, larger trace length N to NNW trending cleats and joints (e.g. Phase 2 joints, Fig. 5a) were
463 reactivated. As the principal stress orientation changed to enable the formation of phase 2 dextral faults
464 (Figure 4c), faulted joints associated with the 1st phase of faulting became reactivated (Figure 8c), with
465 Phase 4 joints preferentially reactivated (Figure 8b, c). Phase 2 joints only became reactivated in the
466 vicinity of self-juxtaposed dextral faults (NW-SE trending feature cutting Figure 8c). The preferential
467 reactivation of specific joint sets could be due to:

- 468 a) Changes in the mechanical properties of lithologies at Spireslack SCM due to mineralisation
469 associated with Phase 1 faults. For example, coal cleats, that previously acted as a weakness
470 in the rock (Li et al., 2016), act as strength inclusions following ankerite mineralisation,
471 enabling barren shear fractures to develop (Figure 3d).
- 472 b) Subtle differences in joint orientation between sets (Figure 8, inset) changes the relative
473 orientation of features to the stress field (e.g. Moir et al., (2010); Zhao and Johnson, (1992)),
474 and alters the stress ratio across the fracture (Chang and Haimson, 2000; Haimson and
475 Chang, 2000).
- 476 c) Differences in mechanical properties of the fracture surface. For example, due to their longer
477 trace length, fracture roughness (Nasseri et al., 2009; Tsang and Witherspoon, 1983) could

478 increase in Phase 1 joints in comparison to smaller trace length Phase 3 or 5 joints (Reed et
479 al., 2008).

480 The fact that some joints show evidence of preferential reactivation and subsequent cementation, while
481 others remain barren, suggests that certain joint sets indicate the past-connectivity of mineral rich fluids
482 through the network, which at Spireslack SCM was dominated by faults (Figure 8). Barren joints
483 typically post-date mineralisation (Peacock, 2001; Peacock and Sanderson, 2018), however, Phase 1
484 and 3 joints at Spireslack are often offset by faults or reactivated as faulted joints (Figure 8). This
485 suggests joints were present at the time of faulting, however, not all joints sets were hydraulically
486 connected to the mineralising fluids. This could be either due to: fluid flow being dominated by vertical
487 flow associated with fault-valve behaviour during slip events (Sibson, 1990, 1992); micro-cataclasite
488 and/or mineralisation along joints that were not visible during field observations or had been weathered
489 out during subsequent groundwater flow; or mineralisation occurred under a stress-induced flow pattern
490 that had a relatively high stress ratio ($k < 3$). This would result in flow becoming channelised along
491 favourably orientated features while those sub-optimally orientated are not dilated and therefore contain
492 no, or very little, flow (Baghbanan and Jing, 2008).

493 Groundwater flow within Carboniferous aquifers is dominated by bed-parallel fracture flow
494 (Dochartaigh et al., 2015). While the combined fault-fracture network across the McDonald limestone
495 displays very high network connectivity ($P_c = 0.96$ to 1.00) and high fracture density ($D = 3.1$ to 5.9
496 f/m^2) (Figure 9, S2), mineralised faults (Figures 5, 6) may act as a baffle or barrier to flow (e.g.
497 (Skurtveit et al., 2015). It is therefore more appropriate to consider the ‘joint network’ when assessing
498 the modern-day network connectivity at the site. While joint intensity increases as fault-intensity
499 increases (Table 3) this is not the case for connectivity. Where faulting intensity was low, joints are well
500 connected (SA1, $P_c = 0.96$). However, as fault intensity increased and the number of faulted joints
501 increases, connectivity drops to $P_c = 0.90$. For example, in SA3, where fault intensity is 1.9 f/m , the
502 connectivity of the joint network drops to $P_c = 0.77$. Additionally, connectivity depends on the
503 orientation of the fractures, with NW trending features being the most connected (Table 3, Figure 9).
504 The modern day stress orientation in Scotland (roughly northerly trending maximum compressive stress
505 (Baptie, 2010; Heidbach et al., 2008)) would act to reduce the aperture of these large trace length joint
506 sets and further reduce the permeability of the network. This leads to the counter-intuitive observation
507 that although joint intensity increases in areas associated with faulting (Table 3), the cementation of
508 faults and faulted joints causes the connectivity of the modern day network in these areas to be lower
509 (Figure 9).



510

511 **Figure 9: Network topology data. Node and branch triangle (after Sanderson & Nixon (2015)) for**
 512 **the joint, fault, and combined fracture networks for the three samples areas shown in Figure 8: a) a**
 513 **node and b) branch data presented by sample area for the fault, joint, and combined networks,**
 514 **and c) branch data by sets, as outlined in S2, to investigate the directionality of network**
 515 **connectivity.**

516 **6.2 The role of lithology on faulting style: self-juxtaposed vs non self-juxtaposed faulting**

517 The internal structure of faults at Spireslack SCM is greatly affected by the level of lithological
518 juxtaposition, with different properties observed for self-juxtaposed faults (Section 4.2.1) and those that
519 cut multiple lithologies (Section 4.2.2). Self-juxtaposed fault-strands cutting lithologies without pre-
520 existing joints are typically relatively planar, develop relay zones, and only display local iron staining
521 along fault planes (e.g. the 6' seat earth; Figure 5a, b). Conversely, in lithologies where pre-existing
522 weaknesses influence the growth of faults, multiple sets of lineations on fault planes and the presence of
523 compound veins provide evidence for multiple slip events (McDonald Limestone; Figure 3a, c, 6b & 8).
524 This suggests that faults in these lithologies initiated as a segmented fault-fracture mesh (Sibson, 1996),
525 with field evidence suggesting mineralising fluid flow in the McDonald limestone and coal occurred as
526 multiple crack-seal events (Figure 3c, e). This implies that self-juxtaposed faults cutting the McDonald
527 limestone and 6' coal at Spireslack behaved in a similar manner to other faults in carbonates with fluid
528 pathways only remaining open for a small amount of time and probably closing following fault slip (c.f
529 Billi et al. 2003; Sibson, 1990, 1992). Mineralised Phase 1 faults that cut multiple lithologies also
530 display multiple slip events (Figure 6c) and matrix (calcite) supported fault breccias located within relay
531 zones (Figure 6d), intersections between Phase 1 and 2 faults (Figure 6c), and at asperities along the
532 principle slip zone (Figure 6a). This suggests fault valve behaviour was also present along non-self-
533 juxtaposed faults (Peacock et al., 2019; Sibson, 1990).

534 Where faults cut multiple lithologies, shale accommodates the rotation of bedding, leading to rotated
535 blocks and multiple generations of curved slickensides (Figure 6). As shale is buried and compressive
536 stresses increase, the ratio of pre-consolidation stress and compaction-related stresses control the
537 behaviour of shales and mud rocks (Yuan et al., 2017; Nygård et al., 2006). As a general rule, shales are
538 ductile during burial, and brittle during exhumation where they experience stresses below the maximum
539 stress they have encountered. Ductile behaviour of the shales at the time of faulting suggests that both
540 phases of faulting occurred prior to maximum burial, which is estimated at <3,000 m at around 60 Ma
541 for the Limestone Coal Formation (Monaghan, 2014).

542 Fault cores at Spireslack SCM also differ between self-juxtaposed faults (Figure 5) and those that cut
543 multiple lithologies (Table 2). Wilkins *et al.* (2001), studying growth of normal faults through jointed
544 lithologies, found similar observations to those at Spireslack SCM with little fault rock development
545 (Figure 3a, 5f), and considerably smaller displacement/length ratios than that expected for faults which
546 do not cut jointed lithologies (Figure 5f, 6a, d). While fault core at Spireslack SCM is typically thin
547 (Table 2), similar to previous studies (e.g. McKay et al., 2019; De Rosa et al., 2018) thickness was
548 found to be highly heterogeneous both along strike and down dip. Much of this variability is caused by

549 the lithological juxtapositions observed across the fault (Figure 7), asperities on the principal slip zone
550 (Figure 6), the degree of folding (Figure 6) and the presence of fault core lenses (Figure 7). In
551 agreement with the fault growth model of Childs et al. (2009), the highly segmented network of self-
552 juxtaposed faults (Figure 8), and differences in fault dip between lithologies (Figure 4d), contribute to
553 the heterogeneity observed in the fault-cores of faults that cut multiple lithologies.

554 Our data demonstrates that the evolution of faults and fault zone structure, and therefore the bulk
555 hydraulic properties of the rock mass at Spireslack SCM, varied both through time and as faults cut
556 multiple lithologies. The abundance of faults within competent lithologies that cannot be traced into
557 shale interbeds suggests faults at Spireslack SCM initiated as segmented fault strands within competent
558 lithologies (e.g. limestones) and the coals (Figures 5, 8), with shale interbeds. They restricted fault
559 growth and instead accommodating ductile deformation. Despite faulting being dominantly strike slip,
560 the oblique orientation of faults to bedding across the site meant that many fault-growth models derived
561 from observations and modelling of normal faults in mechanically layered sequences appear to be valid
562 (e.g. (Childs et al., 1996; Ferrill et al., 2017; Schöpfer et al., 2006, 2007, 2016) . However, it is also
563 clear that the initial segmented fault network within the competent layers was strongly controlled by the
564 presence and evolution of the joints and mineralised fault zones (Figure 8). It is therefore helpful to
565 consider the concept of lithological juxtaposition, the presence and behaviours of shale interbeds, and
566 the relative timing of deformation, when considering the growth and internal structure of fault growth in
567 mechanically layered sequences.

568 **6. Conclusions**

569 The exceptional exposures of the Limestone Coal Formation at Spireslack SCM provides an excellent
570 opportunity to examine the role of lithology and pre-existing structures on fault evolution, internal
571 structure and connectivity. Careful mapping to unpick cross-cutting relationships has revealed a 5 stage,
572 complex geological evolution for the Spireslack SCM succession consisting of two phases of faulting
573 and eight phases of joint development:

574 **Stage 1:** Cleats and multiple sets of joints formed during burial of the fluvial-deltaic host rocks and
575 formation of the regional Muirkirk syncline.

576 **Stage 2:** Sinistral transpression caused the formation of Phase 1 faults, with self-juxtaposed faults
577 laterally restricted by NE trending cleats and Phase 1 and 3 joints. The same transpression preferentially
578 reactivates Phase 2 joints to form faulted joints. Larger faults, which cut multiple lithologies, developed
579 a complex mineralised fault core with multiple slip events.

580 **Stage 3:** Dextral transpression caused the formation of NW trending Phase 2 faults with self-juxtaposed
581 faults restricted by pre-existing joints or cleats, and larger faults restricted by Phase 1 faults. Phase 2
582 faults led to the reactivation of Phase 3 joints and reactivated Phase 1 faulted joints. Where Phase 1 and
583 Phase 2 faults interact, complex zones of deformation develop.

584 **Stage 4:** Paleogene igneous dykes cut across the site, preferentially exploiting Phase 2 faults, and
585 display post intrusion extensional reactivation (**Stage 5**).

586 While the overall fracture density increases around the larger faults, counter-intuitively the modern day
587 network connectivity decreases in these areas due to the cementation of faults and joints.

588 We find that the fault zone internal structure at Spireslack SCM depends on: a) whether the fault is self-
589 juxtaposed or cuts multiple lithologies; b) the presence and ductility of shale layers, which in turns leads
590 to bed-rotation and fault-core lens formation; and c) the orientation of open and mineralised joints/coal
591 cleats at the time of faulting. Self-juxtaposed faults are strongly affected by the orientation, and
592 mineralisation of pre-existing joint-sets and coal cleats, causing them to grow as multiple segmented
593 fault strands within competent lithologies. Self-juxtaposed faults only become well connected where
594 fault intensity is high. Faults that cut multiple lithologies are strongly affected by the presence of shale
595 interbeds and display a complex and heterogenous fault structure with fault length limited by the
596 presence of pre-existing faults. Therefore, it is crucial to appreciate the relative timing of deformation
597 events, concurrent or subsequent cementation and the degree of lithological juxtaposition when
598 considering the mechanical and hydraulic properties of a mechanically stratified succession.

599 Acknowledgements

600 This work was funded through BJA's PhD studentship, supported by the Environmental and Physical
601 Sciences Research Council (EPSRC, award number EP/L016680/1). LMcK is supported by a
602 University of Strathclyde Environmental and Physical Science Research Council (EPSRC) Doctoral
603 Training Partnership (DTP) award (award reference 1904102). We would like to thank Dave Healy for
604 the use of the high-resolution photomontage of the McDonald Limestone dip slope and the British
605 Geological Society for the use of the photomontage of the high wall.

606 **References**

607 Anderson, E. M.: The dynamics of faulting and dyke formation with applications to Britain, Oliver &
608 Boyd, Edinburgh., 1951.

609 Andrews, B. J., Roberts, J. J., Shipton, Z. K., Bigi, S., Tartarello, M. C. and Johnson, G. O.: How do we
610 see fractures? Quantifying subjective bias in fracture data collection, *Solid Earth*, 10(2), 487–516,
611 doi:<https://doi.org/10.5194/se-10-487-2019>, 2019.

612 Baghbanan, A. and Jing, L.: Stress effects on permeability in a fractured rock mass with correlated
613 fracture length and aperture, *Int. J. Rock Mech. Min. Sci.*, 45(8), 1320–1334,
614 doi:<https://doi.org/10.1016/j.ijrmms.2008.01.015>, 2008.

615 Baptie, B.: Seismogenesis and state of stress in the UK, *Tectonophysics*, 482(1–4), 150–159,
616 doi:[10.1016/j.tecto.2009.10.006](https://doi.org/10.1016/j.tecto.2009.10.006), 2010.

617 Bluck, B. J.: Pre-Carboniferous history of the Midland Valley of Scotland, *Trans. R. Soc. Edinb. Earth
618 Sci.*, 75(2), 275–295, doi:[10.1017/S0263593300013900](https://doi.org/10.1017/S0263593300013900), 1984.

619 Bons, P. D., Elburgm, M. . and Gomez-Rivas, E.: A review of the formation of tectonic veins and their
620 microstructures, *J. Struct. Geol.*, 43, 33–62, doi:<https://doi.org/10.1016/j.jsg.2012.07.005>, 2012.

621 Browne, M. A. E. and Monro, S. K.: Evolution of the coal basins of Central Scotland, in *Congrès
622 International de Stratigraphie et de Géologie du Carbonifère*, pp. 1–19, Nanjing University Press,
623 Nanjing, Beijing., 1987.

624 Browne, M. A. E., Dean, M. T., Hall, I. H. S., McAdam, A. D., Monro, S. K. and Chisholm, J. I.: A
625 lithostratigraphical framework for the Carboniferous rocks of the Midland Valley of Scotland,
626 Keyworth, Nottingham: British Geological Survey., 1999.

627 Caldwell, W. G. E. and Young, G. M.: The Cumbrae Islands: A structural Rosetta Stone in the western
628 offshore Midland Valley of Scotland, *Scottish J. Geol.*, 49(2), 117–132, doi:[10.1144/sjg2011-462](https://doi.org/10.1144/sjg2011-462), 2013.

629 Caputo, R.: Evolution of orthogonal sets of coeval extension joints, *Terra Nov.*, 7(5), 479–490,
630 doi:[10.1111/j.1365-3121.1995.tb00549.x](https://doi.org/10.1111/j.1365-3121.1995.tb00549.x), 1995.

631 Caputo, R. and Hancock, P. L.: Crack-jump mechanism and its implications for stress cyclicity during
632 extension fracturing, *J. Geodyn.*, 27(1), 45–60, doi:[10.1016/S0264-3707\(97\)00029-X](https://doi.org/10.1016/S0264-3707(97)00029-X), 1998.

633 Chang, C. and Haimson, B.: True triaxial strength and deformability of the German Continental Deep
634 Drilling Program (KTB) deep hole amphibolite, *J. Geophys. Res. Solid Earth*, 105(B8), 18999–19013,
635 doi:[10.1029/2000jb900184](https://doi.org/10.1029/2000jb900184), 2000.

636 Childs, C., Nicol, A., Walsh, J. J. and Watterson, J.: Growth of vertically segmented normal faults, *J.
637 Struct. Geol.*, 18(12), 1389–1397, doi:[10.1016/S0191-8141\(96\)00060-0](https://doi.org/10.1016/S0191-8141(96)00060-0), 1996.

638 Childs, C., Manzocchi, T., Walsh, J. J., Bonson, C. G., Nicol, A. and Schöpfer, M. P. J.: A geometric
639 model of fault zone and fault rock thickness variations, *J. Struct. Geol.*, 31(2), 117–127,

640 doi:10.1016/j.jsg.2008.08.009, 2009.

641 Coward, M. P.: The effect of Late Caledonian and Variscan continental escape tectonics on basement
642 structure, Paleozoic basin kinematics and subsequent Mesozoic basin development in NW Europe, in
643 Petroleum Geology Conference Proceedings, vol. 4, pp. 1095–1108, Geological Society of London.,
644 <https://doi.org/10.1144/0041095>, 1993.

645 Crider, J. G. and Peacock, D. C. P.: Initiation of brittle faults in the upper crust: A review of field
646 observations, *J. Struct. Geol.*, 26(4), 691–707, doi:10.1016/j.jsg.2003.07.007, 2004.

647 Cruikshank, K. M., Zhao, G. and Johnson, A. M.: Analysis of minor fractures associated with joints and
648 faulted joints, *Journal of Structural Geology*, 13(8), 865-886, [https://doi.org/10.1016/0191-8141\(91\)90083-U](https://doi.org/10.1016/0191-8141(91)90083-U), 1991.

650 Davis, A.: Carboniferous rocks of the Muirkirk, Gass Water and Glenmuir areas of Ayrshire, *Bull Geol
651 Surv GB*, 40, 1–49, 1972.

652 Dean, M. T., Browne, M. A. E., Waters, C. N. and Powell, J. H.: A lithostratigraphical framework for
653 the Carboniferous successions of northern Great Britain (onshore), *Br. Geol. Surv. Res. Rep.*, RR/10/07,
654 174, 2011.

655 Dershowitz, W. S. and Einstein, H. : Characterizing Rock Joint Geometry with Joint System Models,
656 *Rock Mech. Rock Eng.*, 21(1), 21–51, <https://doi.org/10.1007/BF01019674>, 1988.

657 Dochartaigh, B. É. Ó., Macdonald, A. M., Fitzsimons, V. and Ward, R.: Scotland's aquifers and
658 groundwater bodies, *Br. Geol. Surv. Res. Rep.*, OR/15/028, 63 [online] Available from:
659 www.bgs.ac.uk/gsni/ (Accessed 11 October 2019), 2015.

660 Donath, F. A.: Experimental study of shear failure in anisotropic rocks, *Geol. Soc. Am. Bull.*, 72, 985–
661 990, doi:[https://doi.org/10.1130/0016-7606\(1961\)72\[985:ESOSFI\]2.0.CO;2](https://doi.org/10.1130/0016-7606(1961)72[985:ESOSFI]2.0.CO;2), 1961.

662 Donnelly, L. J.: A review of coal mining induced fault reactivation in Great Britain, *Q. J. Eng. Geol.
663 Hydrogeol.*, 39, 5–50, DOI: 10.1144/1470-9236/05-015, 2006.

664 Dunham, K.C.: Geology of the Northern Pennine Orefield Volume 1 Tyne to Stainmore. HMSO,
665 London, UK, 1948.

666 Ellen, R., Callaghan, E., Leslie, A. G. and Browne, M. A. E.: The rocks of Spireslack surface coal mine
667 and its subsurface data: an introduction, *Br. Geol. Surv. Res. Rep.*, OR/16/053, 38, 2016.

668 Ellen, R., Browne, M. A. ., Mitten, A. ., Clarke, S. M., Leslie, A. G. and Callaghan, E.: Sedimentology,
669 architecture and depositional setting of the fluvial Spireslack Sandstone of the Midland Valley,
670 Scotland: insights from the Spireslack surface coal mine, *Geol. Soc. London, Spec. Publ.*, 488, SP488-2,
671 <https://doi.org/10.1144/SP488.2>, 2019.

672 Emeleus, C. H. and Gyopari, M. C.: British Tertiary Igneous Province, Chapman and Hall, London,
673 UK., 1992.

674 Ferrill, D. a. and Morris, A. P.: Dilational normal faults, *J. Struct. Geol.*, 25, 183–196,
675 doi:10.1016/S0191-8141(02)00196-7, 2003.

676 Ferrill, D. A. and Morris, A. P.: Fault zone deformation controlled by carbonate mechanical
677 stratigraphy, Balcones fault system, Texas, *Am. Assoc. Pet. Geol. Bull.*, 92(3), 359–380,
678 doi:10.1306/10290707066, 2008.

679 Ferrill, D. A., McGinnis, R. N., Morris, A. P. and Smart, K. J.: Hybrid failure: Field evidence and
680 influence on fault refraction, *J. Struct. Geol.*, 42, 140–150, doi:10.1016/j.jsg.2012.05.012, 2012.

681 Ferrill, D. A., Morris, A. P., McGinnis, R. N., Smart, K. J., Wigginton, S. S. and Hill, N. J.: Mechanical
682 stratigraphy and normal faulting, *J. Struct. Geol.*, 94, 275–302, doi:10.1016/j.jsg.2016.11.010, 2017.

683 Francis, E. H.: Carboniferous: in CRAIG, in *The Geology of Scotland*, pp. 253–296, Scottish Academic
684 Press, Edinburgh., 1991.

685 George, T. N.: Eustasy and tectonics: Sedimentary rhythms and stratigraphical units in British
686 Dinantian correlation, in *Proceedings of the Yorkshire Geological Society*, vol. 42, pp. 229–262,
687 <https://doi.org/10.1144/pygs.42.2.229>, 1978.

688 Gibson, R. G. and Bentham, P. A.: Use of fault-seal analysis in understanding petroleum migration in a
689 complexly faulted anticlinal trap, Columbus Basin, offshore Trinidad, *Am. Assoc. Pet. Geol. Bull.*,
690 87(3), 465–478, doi:10.1306/08010201132, 2003.

691 Haimson, B. and Chang, C.: A new true triaxial cell for testing mechanical properties of rock, and its
692 use to determine rock strength and deformability of Westerly granite, in *International Journal of Rock
693 Mechanics and Mining Sciences*, vol. 37, pp. 285–296, [https://doi.org/10.1016/S1365-1609\(99\)00106-9](https://doi.org/10.1016/S1365-1609(99)00106-9), 2000.

695 Haszeldine, R. S.: Carboniferous North Atlantic palaeogeography: Stratigraphic evidence for rifting, not
696 megashear or subduction, *Geol. Mag.*, 121(5), 443–463, doi:10.1017/S0016756800029988, 1984.

697 Healy, D., Jones, R. R. and Holdsworth, R. E.: Three-dimensional brittle shear fracturing by tensile
698 crack interaction, *Nature*, 439(7072), 64–67, doi:10.1038/nature04346, 2006.

699 Heidbach, O., Tingay, M., Barth, A., Reinecker, J., Kurfeß, D. and Müller, B.: The world stress map
700 database release, WSM, Rel2008(9) [online] Available from: doi: 10.1594/GFZ, 2008.

701 Holland, M. and Urai, J. L.: Evolution of anastomosing crack–seal vein networks in limestones: Insight
702 from an exhumed high-pressure cell, Jabal Shams, Oman Mountains, *J. Struct. Geol.*, 32(9), 1279–1290,
703 doi:<https://doi.org/10.1016/j.jsg.2009.04.011>, 2010.

704 Jones, R. . and Tanner, P. W. G.: Strain partitioning in transpression zones, *J. Struct. Geol.*, 17(6), 793–
705 802, doi:[https://doi.org/10.1016/0191-8141\(94\)00102-6](https://doi.org/10.1016/0191-8141(94)00102-6), 1995.

706 Kattenhorn, S. A., Aydin, A. and Pollard, D. D.: Joints at high angles to normal fault strike: An
707 explanation using 3-D numerical models of fault-perturbed stress fields, *J. Struct. Geol.*, 22(1), 1–23,
708 doi:10.1016/S0191-8141(99)00130-3, 2000.

709 Knai, T. A. and Knipe, R. J.: The impact of faults on fluid flow in the Heidrun Field, Geol. Soc. Spec.
710 Publ., 147(1), 269–282, doi:10.1144/GSL.SP.1998.147.01.18, 1998.

711 Lăpădat, A., Imber, J., Yielding, G., Iacopini, D., McCaffrey, K. J. W., Long, J. J. and Jones, R. R.:
712 Occurrence and development of folding related to normal faulting within a mechanically heterogeneous
713 sedimentary sequence: A case study from Inner Moray Firth, UK, Geological Society Special
714 Publication, vol. 439, pp. 373–394, <https://doi.org/10.1144/SP439.18>, 2017.

715 Laubach, S. E., Marrett, R. A., Olson, I. E. and Scott, A. R.: Characteristics and origins of coal cleat: a
716 review, Int. J. Coal Geol., 35(1–4), 175–207, doi:10.1016/S0166-5162(97)00012-8, 1998.

717 Laubach, S. E., Olson, J. E. and Cross, M. R.: Mechanical and fracture stratigraphy, Am. Assoc. Pet.
718 Geol. Bull., 93(11), 1413–1426, doi:10.1306/07270909094, 2009.

719 Leeder, M. R.: Upper Palaeozoic basins of the British Isles-Caledonide inheritance versus Hercynian
720 plate margin processes, J. Geol. Soc. London, 139(1980), 479–491, doi:10.1144/gsjgs.139.4.0479,
721 1982.

722 Leeder, M. R.: Recent developments in Carboniferous geology: a critical review with implications for
723 the British Isles and N.W. Europe, Proc. Geol. Assoc., 99(2), 79–100, [https://doi.org/10.1016/S0016-7878\(88\)80001-4](https://doi.org/10.1016/S0016-7878(88)80001-4), 1988.

725 Leslie, A. G., Browne, M. A. E., Cain, T. and Ellen, R.: From threat to future asset—The legacy of
726 opencast surface-mined coal in Scotland, Int. J. Coal Geol., 164, 123–133,
727 doi:10.1016/j.coal.2016.06.017, 2016.

728 Li, Y. W., Zhang, J. and Liu, Y.: Effects of loading direction on failure load test results for Brazilian
729 tests on coal rock, Rock Mech. Rock Eng., 49(6), 2173–2180, doi:10.1007/s00603-015-0841-8, 2016.

730 Long, J. J. and Imber, J.: Geological controls on fault relay zone scaling, J. Struct. Geol., 33(12), 1790–
731 1800, doi:10.1016/j.jsg.2011.09.011, 2011.

732 Lunn, R.J., Willson, J.P., Shipton, Z.K. and Moir, H.: Simulating brittle fault growth from linkage of
733 preexisting structures, Journal of Geophysical Research: Solid Earth, 113(B7),
734 <https://doi.org/10.1029/2007JB005388>, 2008.

735 Manzocchi, T.: The connectivity of two-dimensional networks of spatially correlated fractures, Water
736 Resour. Res., 38(9), 1-1-1–20, doi:10.1029/2000WR000180, 2002.

737 McKay, L., Shipton, Z. K., Lunn, R. J., Andrews, B. J., Raub, T. and Boyce, A. J.: Detailed Internal
738 Structure and Along-Strike Variability of the Core of a Plate Boundary Fault: The Highland Boundary
739 Fault, Scotland, J. Geol. Soc. London., doi:<https://doi.org/10.1144/jgs2018-226>, 2019.

740 Microsoft: “Glenbuck, Aryshire” [1:2,000] (Map). Bing Maps., Aer. Photogr. [online] Available from:
741 <https://www.bing.com/maps/>, 2017.

742 Moir, H.: Modelling fault zone evolution : the effect of heterogeneity, University of Strathclyde., 2010.

743 Moir, H., Lunn, R. J., Shipton, Z. K. and Kirkpatrick, J. D.: Simulating brittle fault evolution from
744 networks of pre-existing joints within crystalline rock, *J. Struct. Geol.*, 32(11), 1742–1753,
745 doi:10.1016/j.jsg.2009.08.016, 2010.

746 Monaghan, A. : The Carboniferous shales of the Midland Valley of Scotland : geology and resource
747 estimation, British Geological Survey for Department of Energy and Climate Change, London, UK.,
748 2014.

749 Mykura, W.: White trap in some Ayrshire Coals, *Scottish J. Geol.*, 1(2), 176–184,
750 doi:10.1144/sjg01020176, 1965.

751 Nasseri, M. H. B., Tatone, B. S. A., Grasselli, G. and Young, R. P.: Fracture toughness and fracture
752 roughness interrelationship in thermally treated westerly granite, *Pure Appl. Geophys.*, 166(5–7), 801–
753 822, doi:10.1007/s00024-009-0476-3, 2009.

754 Nicol, A., Watterson, J., Walsh, J. J. and Childs, C.: The shapes, major axis orientations and
755 displacement patterns of fault surfaces, *J. Struct. Geol.*, 18(2–3), 235–248, doi:10.1016/S0191-
756 8141(96)80047-2, 1996.

757 Nyberg, B., Nixon, C. W. and Sanderson, D. J.: NetworkGT: A GIS tool for geometric and topological
758 analysis of two-dimensional fracture networks, *Geosphere*, 14(4), 1618–1634,
759 doi:10.1130/GES01595.1, 2018.

760 Nygård, R., Gutierrez, M., Bratli, R. K. and Høeg, K.: Brittle-ductile transition, shear failure and
761 leakage in shales and mudrocks, *Mar. Pet. Geol.*, 23(2), 201–212, doi:10.1016/j.marpetgeo.2005.10.001,
762 2006.

763 O'Keefe, J. M. K., Bechtel, A., Christianis, K., Dai, S., DiMichele, W. A., Eble, C. F., Esterle, J. S.,
764 Mastalerz, M., Raymond, A. L., Valentim, B. V., Wagner, N. J., Ward, C. R. and Hower, J. C.: On the
765 fundamental difference between coal rank and coal type, *Int. J. Coal Geol.*, 118, 58–87,
766 doi:10.1016/j.coal.2013.08.007, 2013.

767 Oliver, N. H. S. and Bons, P. D.: Mechanisms of fluid flow and fluid–rock interaction in fossil
768 metamorphic hydrothermal systems inferred from vein-wallrock patterns, geometry and microstructure,
769 *Geofluids*, 1(2), 137–162, doi:<https://doi.org/10.1046/j.1468-8123.2001.00013.x>, 2001.

770 Peacock, D. C. P.: The temporal relationship between joints and faults, *J. Struct. Geol.*, 23(2–3), 329–
771 341, doi:10.1016/S0191-8141(00)00099-7, 2001.

772 Peacock, D. C. P. and Sanderson, D. J.: Structural analyses and fracture network characterisation: Seven
773 pillars of wisdom, *Earth-Science Rev.*, 184(June), 13–28, doi:10.1016/j.earscirev.2018.06.006, 2018.

774 Peacock, D. C. P., Sanderson, D. J. and Rotevatn, A.: Relationships between fractures, *J. Struct. Geol.*,
775 106, 41–53, doi:10.1016/j.jsg.2017.11.010, 2018.

776 Peacock, D. C. P., Rotevatn, A. and Sanderson, D. J.: Brecciation driven by changes in fluid column
777 heights, *Terra Nov.*, 31(1), 76–81, doi:10.1111/ter.12371, 2019.

778 Pei, Y., Paton, D. A., Knipe, R. J. and Wu, K.: A review of fault sealing behaviour and its evaluation in

779 siliciclastic rocks, *Earth-Science Rev.*, 150, 121–138, doi:10.1016/j.earscirev.2015.07.011, 2015.

780 Priest, S. D. and Hudson, J. A.: Estimation of discontinuity spacing and trace length using scanline
781 surveys, *Int. J. Rock Mech. Min. Sci.*, 18(3), 183–197, doi:10.1016/0148-9062(81)90973-6, 1981.

782 Ramsay, J. G.: The crack-seal mechanism of rock deformation, *Nature*, 284(5752), 135–139, 1980.

783 Ranalli, G. and Yin, Z. M.: Critical stress difference and orientation of faults in rocks with strength
784 anisotropies: the two-dimensional case, *J. Struct. Geol.*, 12(8), 1067–1071, doi:10.1016/0191-
785 8141(90)90102-5, 1990.

786 Read, W. A., Browne, M. A. , Stephenson, D. and Upton, B. J. .: Carboniferous, in *The Geology of*
787 *Scotland*, edited by N. H. Trewin, pp. 251–300, Geological Society, London, London, UK., 2002.

788 Reed, B. W., Kumar, M., Minich, R. W. and Rudd, R. E.: Fracture roughness scaling and its correlation
789 with grain boundary network structure, *Acta Mater.*, 56(13), 3278–3289,
790 doi:10.1016/j.actamat.2008.03.019, 2008.

791 Rippon, J., Read, W. A. and Park, R. G.: The Ochil Fault and the Kincardine basin: Key structures in
792 the tectonic evolution of the Midland Valley of Scotland, *J. Geol. Soc. London.*, 153(4), 573–587,
793 doi:10.1144/gsjgs.153.4.0573, 1996.

794 Rippon, J. H., Ellison, R. A. and Gayer, R. A.: A review of joints (cleats) in British Carboniferous
795 coals : indicators of palaeostress orientation, *Proc. Yorksh. Geol. Soc.*, 56(Part 1), 15–30,
796 <https://doi.org/10.1144/pygs.56.1.15>, 2006.

797 Ritchie, J. D., Johnson, H., Browne, M. A. E. and Monaghan, A. A.: Late Devonian-Carboniferous
798 tectonic evolution within the Firth of Forth, Midland Valley: As revealed from 2D seismic reflection
799 data, *Scottish J. Geol.*, 39(2), 121–134, doi:10.1144/sjg39020121, 2003.

800 Roche, V., Homberg, C. and Rocher, M.: Fault nucleation, restriction, and aspect ratio in layered
801 sections: Quantification of the strength and stiffness roles using numerical modeling, *J. Geophys. Res.*
802 *Solid Earth*, 118, 4446–4460, <https://doi.org/10.1002/jgrb.50279>, 2013.

803 Rohrbaugh, J. B., Dunne, W. M. and Mauldon, M.: Estimating fracture trace intensity, density, and
804 mean length using circular scan lines and windows, *Am. Assoc. Pet. Geol. Bull.*, 86(12), 2089–2104,
805 doi:10.1306/61EEDE0E-173E-11D7-8645000102C1865D, 2002.

806 De Rosa, S., Shipton, Z., Lunn, R., Kremer, Y. and Murry, T.: Along-strike fault core thickness
807 variations of a fault in poorly lithified sediments, Miri (Malaysia), *J. Struct. Geol.*, 116, 189–206,
808 doi:<https://doi.org/10.1016/j.jsg.2018.08.012>, 2018.

809 Sanderson, D. J.: Field-based structural studies as analogues to sub-surface reservoirs, in *Geological*
810 *Society Special Publication*, vol. 436, pp. 207–217, Geological Society of London.,
811 <https://doi.org/10.1144/SP436.5>, 2015.

812 Sanderson, D. J. and Nixon, C. W.: The use of topology in fracture network characterization, *J. Struct.*
813 *Geol.*, 72, 55–66, doi:10.1016/j.jsg.2015.01.005, 2015.

814 Sanderson, D. J. and Nixon, C. W.: Topology, connectivity and percolation in fracture networks, *J.
815 Struct. Geol.*, 115(August 2016), 167–177, doi:10.1016/j.jsg.2018.07.011, 2018.

816 Scheiber, T., Fredin, O., Viola, G., Jarna, A., Gasser, D. and Łapińska-viola, R.: Manual extraction of
817 bedrock lineaments from high-resolution LiDAR data : methodological bias and human perception,
818 *GFF*, 137(4), doi:10.1080/11035897.2015.1085434, 2015.

819 Schmatz, J., Vrolijk, P. J. and Urai, J. L.: Clay smear in normal fault zones - The effect of multilayers
820 and clay cementation in water-saturated model experiments, *J. Struct. Geol.*, 32(11), 1834–1849,
821 doi:10.1016/j.jsg.2009.12.006, 2010.

822 Schöpfer, M. P. J., Childs, C. and Walsh, J. J.: Localisation of normal faults in multilayer sequences, *J.
823 Struct. Geol.*, 28(5), 816–833, doi:10.1016/j.jsg.2006.02.003, 2006.

824 Schöpfer, M. P. J., Childs, C. and Walsh, J. J.: Two-dimensional distinct element modeling of the
825 structure and growth of normal faults in multilayer sequences: 2. Impact of confining pressure and
826 strength contrast on fault zone geometry and growth, *J. Geophys. Res. Solid Earth*, 112(10),
827 doi:10.1029/2006JB004903, 2007.

828 Schöpfer, M. P. J., Childs, C., Walsh, J. J. and Manzocchi, T.: Evolution of the internal structure of fault
829 zones in three-dimensional numerical models of normal faults, *Tectonophysics*, 666, 158–163,
830 doi:10.1016/j.tecto.2015.11.003, 2016.

831 Shang, J., Hencher, S. R. and West, L. J.: Tensile Strength of Geological Discontinuities Including
832 Incipient Bedding, Rock Joints and Mineral Veins, *Rock Mech. Rock Eng.*, 49, 4213–4225,
833 doi:<https://doi.org/10.1007/s00603-016-1041-x>, 2016.

834 Sibson, R. H.: Conditions for fault-valve behaviour, edited by R. J. Knipe and E. . Rutter, *Geol. Soc.
835 London, Spec. Publ.*, 54(1), 15–28, doi:10.1144/GSL.SP.1990.054.01.02, 1990.

836 Sibson, R. H.: Implications of fault-valve behaviour for rupture nucleation and recurrence,
837 *Tectonophysics*, 211(1–4), 283–293, doi:10.1016/0040-1951(92)90065-E, 1992.

838 Sibson, R. H.: Structural permeability of fluid-driven fault-fracture meshes, *J. Struct. Geol.*, 18(8),
839 1031–1042, doi:10.1016/0191-8141(96)00032-6, 1996.

840 Skurtveit, E., Torabi, A., Alikarami, R. and Braathen, A.: Fault baffle to conduit developments:
841 reactivation and calcite cementation of deformation band fault in aeolian sandstone, *Pet. Geosci.*, 21(1),
842 3–16, doi:<https://doi.org/10.1144/petgeo2014-031>, 2015.

843 Soden, A. M. and Shipton, Z. K.: Dilational fault zone architecture in a welded ignimbrite: The
844 importance of mechanical stratigraphy, *J. Struct. Geol.*, 51, 156–166, doi:10.1016/j.jsg.2013.02.001,
845 2013.

846 Soliva, R. and Benedicto, A.: Geometry, scaling relations and spacing of vertically restricted normal
847 faults, *J. Struct. Geol.*, 27(2), 317–325, doi:10.1016/j.jsg.2004.08.010, 2005.

848 Soper, N. J., Strachan, R. A., Holdsworth, R. E., Gayer, R. A. and Greiling, R. O.: Sinistral
849 transpression and the Silurian closure of Iapetus, *J. Geol. Soc. London*, 149, 871–880,

850 doi:<https://doi.org/10.1144/gsjgs.149.6.0871>, 1992.

851 Thomas, L.: *Coal Geology*, Second., Wiley-Blackwell, Chichester., 2013.

852 Tsang, Y. W. and Witherspoon, P. A.: The dependence of fracture mechanical and fluid flow properties
853 on fracture roughness and sample size, *J. Geophys. Res.*, 88(B3), 2359, doi:10.1029/JB088iB03p02359,
854 1983.

855 Turichshev, A. and Hadjigeorgiou, J.: Triaxial compression experiments on intact veined andesite, *Int.*
856 *J. Rock Mech. Min. Sci.*, 86, 179–193, doi:<https://doi.org/10.1016/j.ijrmms.2016.04.012>, 2016.

857 Turichshev, A. and Hadjigeorgiou, J.: Quantifying the effects of vein mineralogy, thickness, and
858 orientation on the strength of intact veined rock, *Eng. Geol.*, 226, 199–208,
859 doi:<https://doi.org/10.1016/j.enggeo.2017.06.009>, 2017.

860 Underhill, J. R., Monaghan, A. A. and Browne, M. A. E.: Controls on structural styles, basin
861 development and petroleum prospectivity in the Midland Valley of Scotland, *Mar. Pet. Geol.*, 25(10),
862 1000–1022, doi:10.1016/j.marpetgeo.2007.12.002, 2008.

863 Virgo, S., Abe, S. and Urai, J. L.: Extension fracture propagation in rocks with veins: Insight into the
864 crack-seal process using Discrete Element Method modeling, *J. Geophys. Res. Solid Earth*, 118(10),
865 5236–5251, doi:<https://doi.org/10.1002/2013JB010540>, 2013.

866 Virgo, S., Abe, S. and Urai, J. L.: The evolution of crack seal vein and fracture networks in an evolving
867 stress field: Insights from Discrete Element Models of fracture sealing, *J. Geophys. Res. Solid Earth*,
868 119(12), 8709–8727, doi:<https://doi.org/10.1002/2014JB011520>, 2014.

869 Walsh, J. J., Nicol, A. and Childs, C.: An alternative model for the growth of faults, *J. Struct. Geol.*,
870 24(11), 1669–1675, doi:10.1016/S0191-8141(01)00165-1, 2002.

871 Wilkins, S. J. and Gross, M. R.: Normal fault growth in layered rocks at Split Mountain, Utah:
872 Influence of mechanical stratigraphy on dip linkage, fault restriction and fault scaling, *J. Struct. Geol.*,
873 24(9), 1413–1429, doi:10.1016/S0191-8141(01)00154-7, 2002.

874 Wilkins, S. J., Gross, M. R., Wacker, M., Eyal, Y. and Engelder, T.: Faulted joints: Kinematics,
875 displacement-length scaling relations and criteria for their identification, *J. Struct. Geol.*, 23(2–3), 315–
876 327, doi:10.1016/S0191-8141(00)00098-5, 2001.

877 Woodcock, N. H. and Mort, K.: Classification of fault breccias and related fault rocks, *Geol. Mag.*,
878 145(3), 435–440, doi:10.1017/S0016756808004883, 2008.

879 Yielding, G., Lykakis, N. and Underhill, J. R.: The role of stratigraphic juxtaposition for seal integrity
880 in proven CO₂ fault-bound traps of the Southern North Sea, *Pet. Geosci.*, 17(2), 193–203,
881 doi:10.1144/1354-0793/10-026, 2011.

882 Yuan, Y. S., Jin, Z. J., Zhou, Y., Liu, J. X., Li, S. J. and Liu, Q. Y.: Burial depth interval of the shale
883 brittle–ductile transition zone and its implications in shale gas exploration and production, *Pet. Sci.*,
884 14(4), 637–647, doi:10.1007/s12182-017-0189-7, 2017.

885 van der Zee, W. and Urai, J. L.: Processes of normal fault evolution in a siliciclastic sequence: A case
886 study from Miri, Sarawak, Malaysia, *J. Struct. Geol.*, 27(12), 2281–2300,
887 doi:10.1016/j.jsg.2005.07.006, 2005.

888 Zhao, G. and Johnson, A. M.: Sequence of deformations recorded in joints and faults, Arches National
889 Park, Utah, *J. Struct. Geol.*, 14(2), 225–236, doi:10.1016/0191-8141(92)90059-6, 1992.

890